Systematic catalog of Martian convective vortices observed by InSight

K. Onodera[1], K. Nishida[1], T. Kawamura[2], N. Murdoch[3], M. Drilleau[3], R. Otsuka[4,5], R. Lorenz[6], A. Horleston[7], R. Widmer-Schnidrig[8], M. Schimmel[9], S. Rodriguez[2], S. Carrasco[10], S. Tanaka[4,5], C. Perrin[11], P. Lognonné[2], A. Spiga[12], D. Banfield[13], M. Panning[14], W. B. Banerdt[14]

[1]Earthquake Research Institute, The University of Tokyo, Tokyo, Japan.
[2]Université Paris Cité, Institut de Physique du Globe de Paris, CNRS, Paris, France
[3]Institut Supérieur de l'Aéronautique et de l'Espace (ISAE-SUPAERO), Université de Toulouse, Toulouse, France
[4]Department of Complexity Science and Engineering, The University of Tokyo, Chiba, Japan
[5]Institute of Space and Astronautical Science, Japan Aerospace Exploration Agency, Kanagawa, Japan
[6]Johns Hopkins University Applied Physics Laboratory, Maryland, USA
[7]School of Earth Sciences, University of Bristol, Bristol, UK
[8]Black Forest Observatory, Wolfach, Germany
[9]Geociencias Barcelona, Barcelona, Spain
[10]Bensberg Observatory, University of Cologne, Bergisch Gladbach, Germany
[11]Nantes Université, Université d'Angers, Le Mans Université, CNRS, UMR 6112, Laboratoire de Planétologie et Géosciences, UAR 3281, Observatoire des Sciences de l'Univers de Nantes Atlantique, Nantes, France
[12]Laboratoire de Météorologie Dynamique/Institut Pierre-Simon Laplace (LMD/IPSL), Centre National de la Recherche Scientifique (CNRS), Sorbonne Université, Paris, France
[13]Cornell Center for Astrophysics and Planetary Science, Cornell University, Ithaca, NY, USA
[14]Jet Propulsion Laboratory, California Institute of Technology, Pasadena, CA, USA

Key Points:

- We investigated the Martian convective vortices observed by InSight's seismometer and meteorological instruments.
- We quantitatively characterized the observed convective vortices and compiled the evaluated parameters as a catalog.
- With the cataloged parameters, we performed a compliance analysis and evaluated the ground rigidity at the InSight landing site.

Corresponding author: Keisuke Onodera, `onodera@eri.u-tokyo.ac.jp`

Abstract

Convective vortices (whirlwinds) and dust devils (dust-loaded vortices) are one of the most common phenomena on Mars, observable on a daily basis. They reflect the local thermodynamical structure of the atmosphere and are the driving force of the dust cycle. Additionally, they cause an elastic ground deformation, which is useful for retrieving the subsurface rigidity. Therefore, investigating Martian convective vortices with the right instrumentation can lead to a better understanding of the Martian atmospheric structures as well as the subsurface physical properties. In this study, we quantitatively characterized the convective vortices detected by NASA's InSight mission ($\sim$13,000 events) using both meteorological (e.g., pressure, wind speed, temperature) and seismic data. The evaluated parameters, such as the signal-to-noise ratio, event duration, asymmetricity of pressure drop profiles, and cross-correlation coefficient between seismic and pressure signals, are compiled as a catalog. To demonstrate how our catalog can contribute to scientific investigations, we show two analysis results about (i) asymmetrical features seen in the vortex-related pressure drops and (ii) atmospheric-ground interaction to retrieve the subsurface physical properties.

Plain Language Summary

As frequently observed on Earth, whirlwinds (convective vortices) or dust devils (dust-loaded vortices) are also seen on Mars. These are one of the smallest meteorological phenomena and are useful to better illustrate what is going on in the near-surface atmosphere. Because dust devils have a strong influence on lander operations (e.g., dust accumulation on a solar panel), it is important to investigate this phenomenon. Recently, NASA's InSight succeeded in installing the meteorological and geophysical packages in the western part of Elysiumu Planitia on Mars. That brought us, in particular, meteorological data with an extremely high temporal resolution, which has never been realized in past missions, contributing to resolving local phenomena such as convective vortices. Moreover, the combination with the seismic data opened the way to the study of "atmosphere-ground coupling", enabling us to evaluate the subsurface physical properties. In this study, using InSight's meteorological (e.g., pressure, air temperature) and seismic data, we quantitatively characterize convective vortices detected by InSight to understand this phenomenon from both meteorological and geophysical aspects. This report includes (i) how we quantified each vortex, (ii) the catalog format including the evaluated parameters, and (iii) some examples of scientific analysis using our catalog.

1 Introduction

NASA's Interior Exploration using Seismic Investigations, Geodesy and Heat Transport (InSight) mission operated on Mars from 2018 to 2022, conducting quasi-continuous seismic and meteorological observations for almost three years of that time. These observations produced many discoveries and made great progress in Martian science, such as the detection of marsquakes, the construction of the internal structure model, and new insights into atmospheric activities (e.g., Banerdt et al., 2020; Lognonné et al., 2020; Giardini et al., 2020; Banfield et al., 2020; Spiga et al., 2021; Stähler et al., 2021; Knapmeyer-Endrun et al., 2021; Khan et al., 2021).

In this study, we pay special attention to the convective vortices or dust devils, which are one of the most common atmospheric phenomena on Mars (e.g., Ellehoj et al., 2010; Reiss et al., 2014; Martínez et al., 2017). The quasi-continuous and high temporal resolution data from InSight plays an important role in improving our knowledge of the local-scale meteorological phenomena on Mars — which was not performed in past missions (e.g., Martínez et al., 2017; Spiga et al., 2018; Banfield et al., 2020; Spiga et al., 2021).

As convective vortices strongly reflect the thermodynamical structure of the local atmosphere, they are useful to capture near-surface atmospheric activities. Also, convective vortices with dust lifting (i.e., dust devils) are a pivotal mechanism of dust particle transportation from the ground to the atmosphere (e.g., Newman et al., 2021; Bila et al., 2020). Another important aspect of the convective vortex is the coupling with the ground (atmosphere-ground interaction). The elastic ground deformation related to pressure perturbations has been observed on Earth (e.g., Sorrells, 1971; Sorrells et al., 1971; Sorrells & Goforth, 1973), including the specific case of a dust devil (Lorenz et al., 2015). The vortex-generated ground deformation was expected to also occur on Mars (e.g., Kenda et al., 2017; Murdoch et al., 2017). Owing to the simultaneous observations of the seismometer and barometer of the InSight mission (e.g., Banerdt et al., 2020), the same phenomenon was also detected on Mars. That allowed us to investigate the subsurface rigidity by measuring the ground deformations caused by transient atmospheric pressure variations (e.g., Banerdt et al., 2020; Lognonné et al., 2020; Kenda et al., 2020; Murdoch et al., 2021). Thus, studying the convective vortex or dust devil is important to push forward our understanding of Martian meteorology, subsurface geology, and atmosphere-ground interactions.

The InSight observations up to Sol 900 (a Sol is a Martian day) brought us about 13,000 pressure drop events (see Spiga et al. (2021) for the details of the detection algorithm). Based on the pressure profile features observed both on Earth and Mars (e.g., sudden pressure drops with amplitudes of 0.1 – 10 Pa and event duration of several seconds to several tens of seconds), these events are considered to be convective vortices (Murphy et al., 2016; Spiga et al., 2021; Lorenz et al., 2021; Chatain et al., 2021). The initial description of some of these observations has been summarized by Banfield et al. (2020) ($\sim$ Sol 200) and Spiga et al. (2021) ($\sim$ Sol 400) from a meteorological aspect and by Lorenz et al. (2021) ($\sim$ Sol 400) focusing both meteorological and seismic observations. The motivation of this study is to give a description of all the detected pressure drop events up to Sol 900, which provides us with many more events for analysis than before, and to provide constructive information for future studies on the Martian convective vortices.

In this paper, followed by a general summary of the convective vortices observed by InSight, we describe how to characterize the observed convective vortices in a quantitative way. In addition to the meteorological aspect, by computing the cross-correlation between the pressure and seismic data, we also discuss the atmosphere-ground interaction. In the end, we provide two examples of the application of our catalog to the scientific discussion: (i) the relation between vortex structure and asymmetricity of pressure drop profile and (ii) the subsurface rigidity derived through compliance analysis.

2 Temporal distribution and size-frequency distribution of the observed convective vortices

Figure 1a shows the temporal distribution of the convective vortices detected with the algorithm proposed by Spiga et al. (2021). The time evolution of atmospheric pressure, air temperature, wind speed, and wind direction are also shown for comparison in Figures 2a-d, where the blank areas correspond to the periods of the conjunction or times when the respective instruments were turned off. Based on both observations and numerical simulations, it is considered that convective vortices are formed mostly when the atmosphere gets turbulent in the daytime due to the heat input by the Sun on the surface. Almost all the vortices have been observed during the daytime at the InSight landing site (Figure 1a and c), when there is a strong temperature gradient between the Martian ground and the atmosphere. Generally, the vortices were detected between 9 – 16 h in Local True Solar Time (LTST) when the atmospheric turbulence was vigorous, which can be seen in the daily variations of the meteorological data (Figures 2a-d). Regarding the seasonal variations (Figure 1c), we observe the annual tendency that the event number increases from winter to spring, is relatively stable during summer, decreases at the beginning of autumn, and then spikes at the transition from autumn to winter. Chatain et al. (2021) investigated the seasonal variations in local turbulence and defined five seasons (Season 1 - 5) besides normally used ones. According to their results, the Martian atmosphere gets turbulent in Season 5, which is confirmed as the rapid increase in the number of vortices. See Chatain et al. (2021) for details about the seasonal variations of the Martian atmospheric activity.

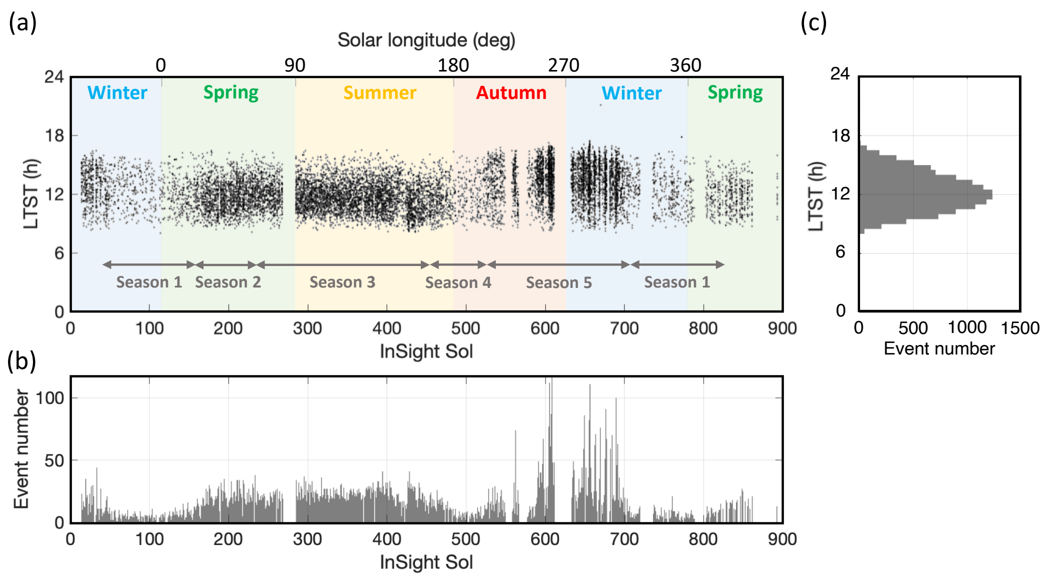

Figure 1. (a) Temporal distribution of the detected convective vortices. Each black point shows a detected vortex. The vertical axis shows the Local True Solar Time (LTST), the bottom horizontal axis shows the InSight sol and the top horizontal axis shows the solar longitude. The different background color indicates different seasons. In addition to ordinarily used seasons, we show "Seasons 1 - 5" proposed by Chatain et al. (2021) based on turbulence tendency over a Martian year. (b) Histogram of the detected events per sol. (c) Histogram of the detected events for every hour.

There are a smaller number of detections of pressure drops at night (Chatain et al., 2021), consistent with past missions (Phoenix and Curiosity) that have also observed occasional night-time pressure drops (e.g., Ellehoj et al., 2010; Ordonez-Etxeberria et al., 2018). Ellehoj et al. (2010) suggested that these events were caused by the interaction of the atmosphere and the local topographies, and the observations by other missions support this idea. For example, many night-time events were confirmed at Gale crater (the Curiosity landing site) which has a complex local topography (e.g., Ordonez-Etxeberria et al., 2018). On the contrary, few night-time events were observed at the landing site of Mars Pathfinder, where the topography is relatively smooth and flat (e.g., Kahanpää et al., 2016). Since the InSight landing site is also smooth and flat (e.g., Golombek et al., 2017, 2020), a small number of detections of night-time events (Chatain et al., 2021) appear consistent with this past interpretation.

Figure 3 summarizes the cumulative size-frequency distribution (CSFD) of pressure drops observed by the past and ongoing missions carrying a barometer (i.e., Mars Pathfinder, Phoenix, Curiosity, InSight, and Perseverance; Murphy & Nelli, 2002; Ellehoj et al., 2010; Ordonez-Etxeberria et al., 2018; Banfield et al., 2018; Hueso et al., 2023). The CSFD data for Mars Pathfinder, Phoenix, Curiosity, and Perseverance were retrieved from previous works (Murphy & Nelli, 2002; Ellehoj et al., 2010; Ordonez-Etxeberria et

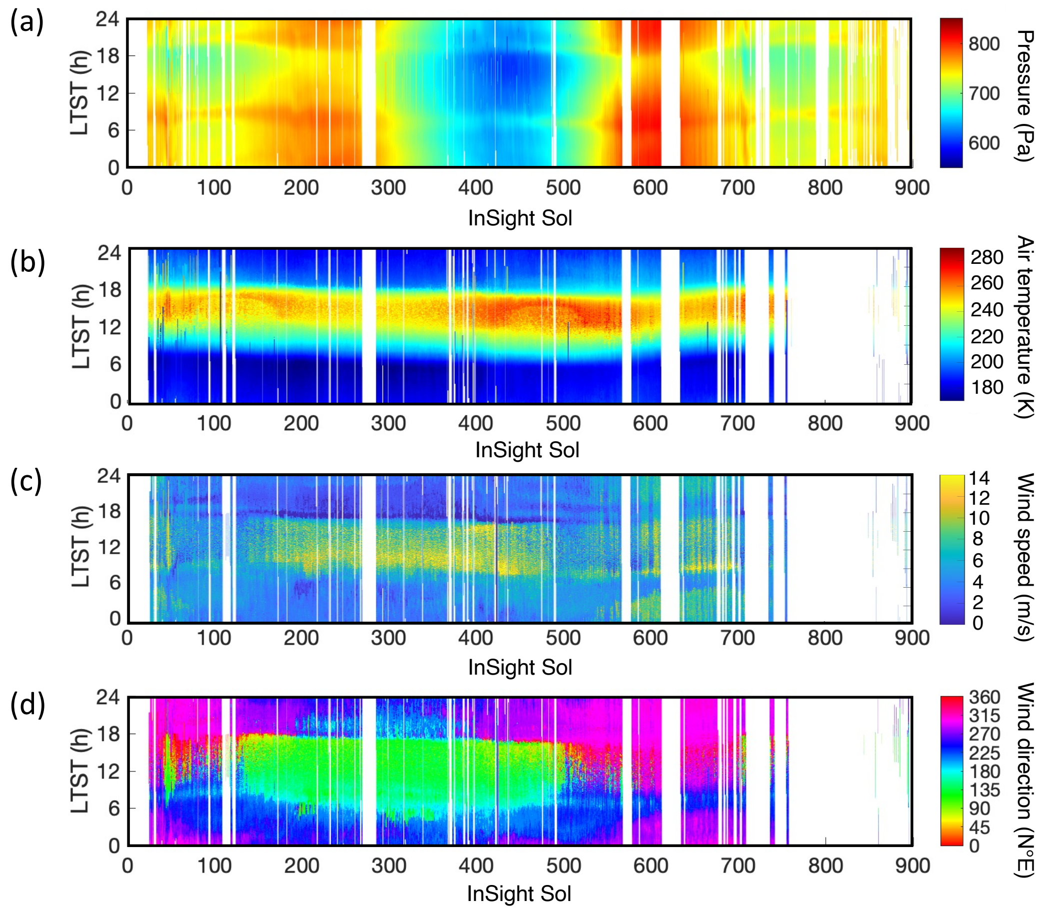

Figure 2. Diurnal and seasonal variations of (a) atmospheric pressure, (b) air temperature, (c) wind speed, and (d) wind direction.

al., 2018; Hueso et al., 2023), and then the power-law fitting was performed using the data between 0.65 and 1.8 Pa (Figure 3). Following the idea of Ordonez-Etxeberria et al. (2018), the cumulative number is corrected to "events per sol" because the observation period differs from mission to mission, which allows us to perform a direct comparison. Interestingly, comparing InSight's CSFD with those of other missions, InSight detected more events than any other missions (Figure 3), which is in agreement with Spiga et al. (2021) and Newman et al. (2022) and contrary to what was presented by Jackson (2022). The InSight's CSFD at smaller pressure drops ($<$ 1.8 Pa) can be fitted with a power law with a -2 slope, which is consistent with others except for Curiosity (slope is -3). The discrepancy between Curiosity's observations with others has been explained by the effect of the shorter Planetary Boundary Layer (PBL) within Gale crater ($\sim$ 2 km) compared to the outside of the crater (8 – 10 km) (Ordonez-Etxeberria et al., 2018) or other landing sites (e.g., 5 – 8 km at InSight landing site; Spiga et al., 2021). When the PBL gets shorter, it becomes more difficult to develop convective vortices in the same way as at the other landing sites, resulting in the lack of larger pressure drop events ($>$ 1 – 2 Pa). Looking at those CSFDs with a slope of -2, we found a kink where the profile starts to be off the trend. Building on the discussion by Ordonez-Etxeberria et al. (2018), this cut-off pressure value might be determined by the PBL height at each landing site. Since recent missions such as InSight and Perseverance provide us with continuous meteorological recordings with high-temporal resolution ($\sim$ 10 Hz), future studies could deepen this topic by making the best of these two missions' data.

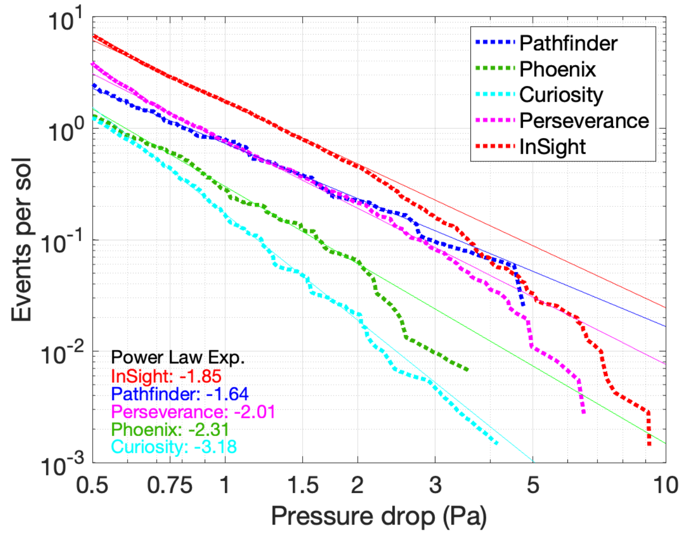

Figure 3. Comparison of the cumulative size-frequency distribution of pressure drops per sol between the past and ongoing Mars missions corrected for observation time bias (dotted profiles). The solid lines represent the fitted curves between 0.65 and 1.8 Pa with a power law. The exponents are shown in the bottom legend.

3 Dataset

We focus on the 12,569 convective vortices detected with the same method used by previous studies (e.g., Spiga et al., 2021; Chatain et al., 2021). The event list can be found at Onodera (2023a), where the events' occurrence time in both UTC and Sol with local time, and the maximum (negative) amplitude of the pressure drop are summarized. This study covers the observation period up to Sol 900 during which the pressure data was quasi-continuously recorded. After that time, the pressure and wind data are recorded so sparsely that few events are recorded, and correcting for sampling biases becomes difficult.

For every detected event, we cut out the 20 min time traces centered at the maximum pressure drop for seismic (velocity and acceleration data) and meteorological data (pressure, wind speed, wind direction, and air temperature) if each data were recorded.

In the following analysis, we use the seismic and pressure data sampled at the nominal sampling rate — 10 sps (sample per second) for pressure data and 20 sps for seismic data. Concerning the wind speed, wind direction, and air temperature data, we made use of 0.1, 0.5, or 1.0 sps data as long as either of them is available. The channel list for respective data is shown in Table 1.

Table 1. Channel list for respective instruments. Readers may refer Onodera (2023b) for removing the instrumental response from the raw seismic data (i.e., converting the digital unit into a physical unit such as m/s).

Instrument	Sampling rate (sps)	Unit	Channel name
Seismometer	20	Digital Unit	XB.ELYSE.02.BHU XB.ELYSE.02.BHV XB.ELYSE.02.BHW
Pressure sensor	10	Pa	XB.ELYSE.13.BDO
Wind sensor (Direction)	0.1 0.5 1.0	N°E	XB.ELYSE.33.VWD XB.ELYSE.30.VWD XB.ELYSE.30.LWD
Wind sensor (Speed)	0.1 0.5 1.0	m/s	XB.ELYSE.33.VWS XB.ELYSE.30.VWS XB.ELYSE.30.LWS
Air temperature	0.1 0.5 1.0	K	XB.ELYSE.33.VKO XB.ELYSE.30.VKO XB.ELYSE.30.LKO

4 Parameters retrieved from the convective vortices observed by InSight

4.1 Signal-to-noise ratio of ground acceleration and air pressure

The signal-to-noise ratio (SNR) is a useful parameter to judge the data quality, and we calculated it for the time series recorded by VBB (Very Broad-Band seismometer; Lognonné et al., 2019) and PS (Pressure Sensor; Banfield et al., 2018) at various frequency bands. The frequency bands are defined as follows: Band 1 (0.01 – 0.05 Hz), Band 2 (0.05 – 0.1 Hz, Band 3 (0.1 – 0.5 Hz), Band 4 (0.5 – 1.0 Hz), and Band 5 (1.0 – 2.0 Hz). In the respective frequency bands, the SNR was estimated by taking the ratio of the peak signal amplitude due to the encounter of a vortex over the background noise signal, that is:

$$SNR = \frac{S_{peak}}{S_{noise}}, \tag{1}$$

where S_{peak} is the absolute value of the peak signal of the detrended and filtered time series within the time window ±150 s from the event time defined by Spiga et al. (2021), and S_{noise} is the noise signal — the average of the absolute value of the detrended and filtered time series within the time window −450 to −150 s (i.e., before the encounter of a convective vortex). Examples of the vertical ground acceleration and the pressure data at the encounter of a convective vortex are shown in Figures 4a-b. Basically, the SNR gets lower as the frequency band becomes higher due to the increase of the contribution from the small turbulence and/or instrumental noises.

4.2 Ambient wind speed, wind direction, and air temperature

The evaluation of the ambient environment is important for understanding the vortices' advection because the vortices are considered to be transported by the ambient winds (e.g., Spiga et al., 2021; Perrin et al., 2020). As the wind and temperature drastically change at the encounter of the vortices at the InSight landing site, we assess the ambient wind speed, wind direction, and air temperature using the 5-min time window (from

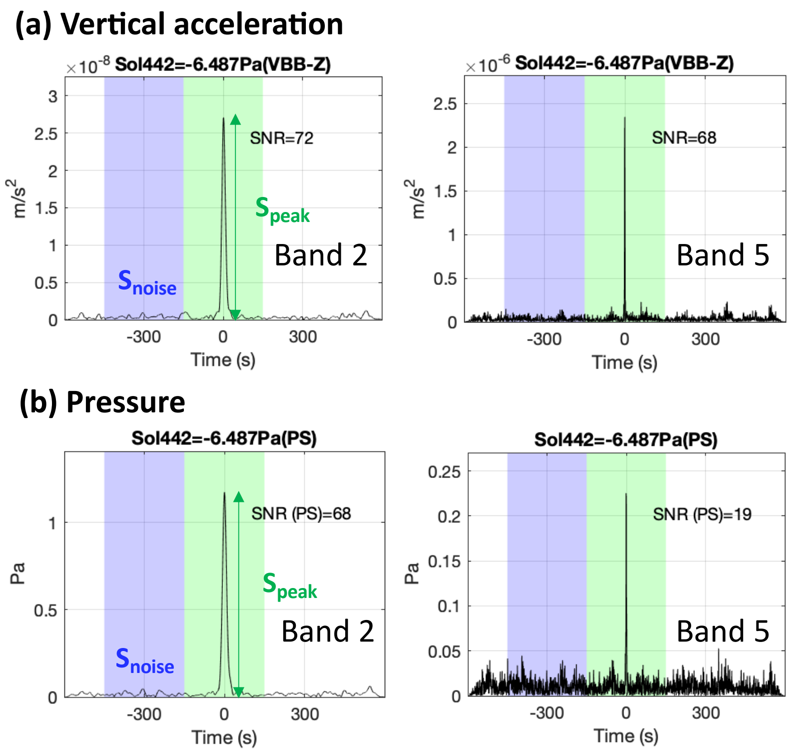

Figure 4. (a) Time series of the absolute value of the vertical acceleration recorded by VBB at the frequency of (left) Band 2 (0.05 – 0.1 Hz) and (right) Band 5 (1.0 – 2.0 Hz). (b) Time series of the absolute value of the pressure data at the frequency of (left) Band 2 (0.05 – 0.1 Hz) and (right) Band 5 (1.0 – 2.0 Hz). Each time series is centered at the maximum point of the pressure drop.

-150 s to $-450s$) prior to each vortex encounter (Figure 5a). The average and standard deviation values are stored in our catalog.

As described by Banfield et al. (2018) and Spiga et al. (2021), the accuracy for the measurements are 1 m/s, 22.5°, and 5 K for wind speed, wind direction, and air temperature, respectively. Thus, in the analysis, one should keep in mind that these factors need to be taken into account depending on the individual interests and research objectives. Also, it is important to note that the wind speed measurement gets unreliable when it becomes smaller than 2.8 m/s or exceeds 20 m/s (e.g., Banfield et al., 2018; Spiga et al., 2021).

Figure 5b shows the histogram of each environmental factor (ambient wind speed, wind direction, and air temperature) estimated using the time window prior to the encounters of all convective vortices we used. The population shows the highest values at 9 m/s for the ambient wind speed, 135 N°E or 300 N°E for the ambient wind direction, and 240 – 250 K for the ambient air temperature. These results are consistent with the general trend seen in Figures 1b-d, meaning the ambient environments were appropriately evaluated with our method. Note that the double peaks in wind direction are relevant to the seasonal variations, which had been numerically predicted before the landing (Spiga et al., 2018) and confirmed by the InSight observations as shown in Figure 2d. 300 N°E corresponds to “Season 5” in Figure 1a and 135 N°E is for other seasons.

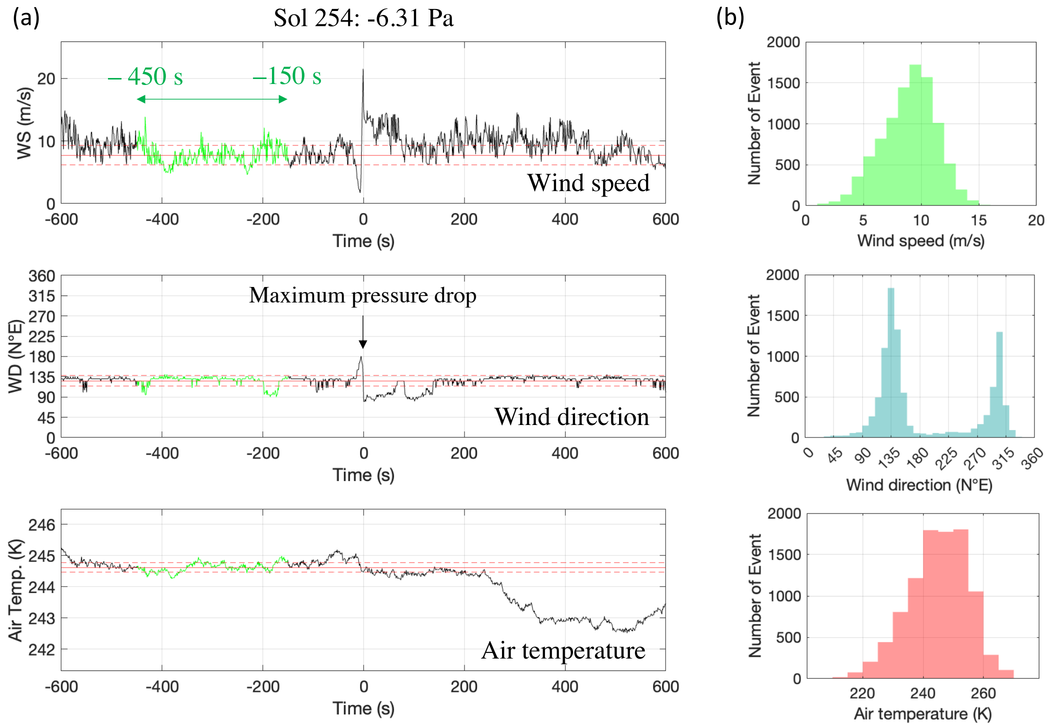

Figure 5. (a) An example of InSight's wind and air temperature data observed around a single pressure drop on Sol 254. From top to bottom, 20 min time traces for wind speed, wind direction, and air temperature are shown (black profiles). 0 s corresponds to the maximum pressure drop time. The average (red solid line) and standard deviation (red broken lines) are computed for the time window between −150 s and −450 s shown in green. (b) Histograms of the ambient wind speed (top), wind direction (middle), and air temperature (bottom) estimated for each vortex event in our catalog.

4.3 Cross-correlation between seismic and pressure data

To quantitatively assess the ground response to atmospheric pressure perturbations, we computed the cross-correlation coefficient between the seismic and pressure data. As reported by previous works (e.g., Kenda et al., 2020; Garcia et al., 2020), the correlation value varies depending on frequency; thereby we evaluated it for the five frequency bands defined in Section 4.1.

The pressure and seismic data being recorded at different sampling rates by individual instruments (PS: 10 sps and VBB: 20 sps), we first resampled the pressure data to synchronize both time stamps. The synchronization was performed by upsampling the PS data from 10 sps to 80 sps in the frequency domain with zero padding. Then, the interpolation with spline fit and downsampling to 20 sps were performed in the time domain using the time stamp of the VBB data. This procedure gave us the pressure data synchronized with the seismic data (Figure 6a).

To put the equal weight in frequency, we divided the pressure spectra with their absolute amplitude, that is, whitening (see the black and blue spectra in Figure 6b). Then, performing the inverse Fourier transform gave us the pressure time traces enhancing phase information (blue waveform in Figure 6b). The same process was applied to the VBB data.

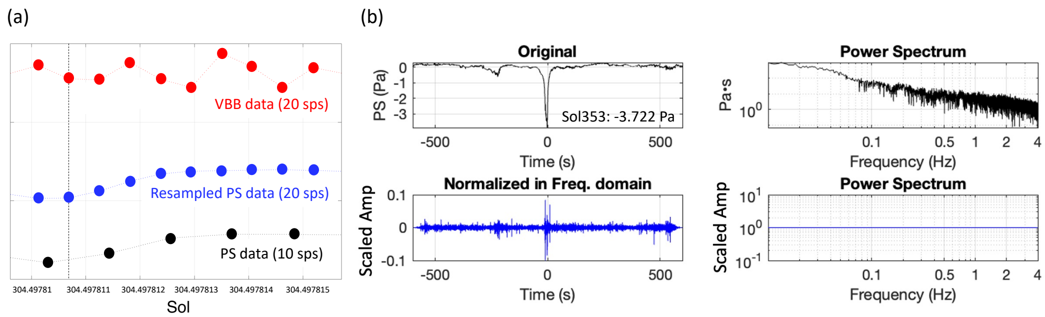

Figure 6. (a) Comparison of pressure data before and after resampling with VBB recorded at the same time period. The black, red, and blue plots correspond to the original PS data (10 sps), the VBB data (20 sps), and the resampled PS data (20 sps), respectively. For better visualization, each profile was scaled and/or an offset was added. (b) Time trace and spectrum of pressure data before (black) and after (blue) normalization process in the frequency domain. See the details in Section 4.3

The whitened seismic and pressure data were bandpass filtered with the 4th order Butterworth filter at Band 1 through Band 5, meaning that there are five pairs of time series for computing cross-correlation at various frequency ranges. An example of the filtered time traces is presented in Figures 7a-b. Note that the time window varies depending on the frequency to make the wavenumber consistent in each band. In this study, we defined the time window $t_{w,j}$ as:

$$t_{w,j} = 10/\overline{f_j} \quad (j = 1, 2, ..., 5), \tag{2}$$

where $\overline{f_j}$ is the average frequency at j-th frequency band. In the following, we use these processed signals for the evaluation of the correlation between ground response and pressure perturbations.

At the five frequency bands, we calculated the cross-correlation for the following combinations:

1. the horizontal acceleration (North or East) and the $\pi/2$-phase shifted pressure signal,
2. the vertical acceleration and the pressure signal,
3. the horizontal velocity (North or East) and the pressure signal,
4. the vertical velocity and the $\pi/2$-phase shifted pressure signal.

The phase shift is considered for cases 1 and 4 following Sorrells' theory (e.g., Sorrells, 1971; Kenda et al., 2020). In the theory, the relation between the ground velocity and the pressure perturbation is expressed as:

$$\begin{aligned} v_z(\omega) &= -2ic\tfrac{1-\nu^2}{E}P(\omega), \\ v_h(\omega) &= c\tfrac{(1+\nu)(1-2\nu)}{E}P(\omega), \end{aligned} \tag{3}$$

where v_z, v_h, P are the spectra of the vertical and horizontal ground velocities and pressure, ω is the angular frequency, c is the advection speed of a vortex — usually approximated as the ambient wind speed (Kenda et al., 2020), i is the imaginary unit, ν is Poisson's ratio, and E is Young's modulus. The first expression in Equation 3 corresponds to case 4, where $iP(\omega)$ requires the $\pi/2$-phase shift to make the pressure signal in phase with the vertical ground velocity. In Section 5.2, we will investigate the subsurface rigidity using this theory.

By taking the cross-correlations for the four combination cases listed above, we obtained the maximum and minimum values of the cross-correlation coefficient and the corresponding lag times at the respective frequency ranges (Figure 7c). Since the correlation coefficient helps us evaluate the quality of the atmosphere-ground coupling (e.g., Kenda et al., 2020), we can use it as a criterion for selecting the better events for the compliance analysis as discussed in Section 5.2.

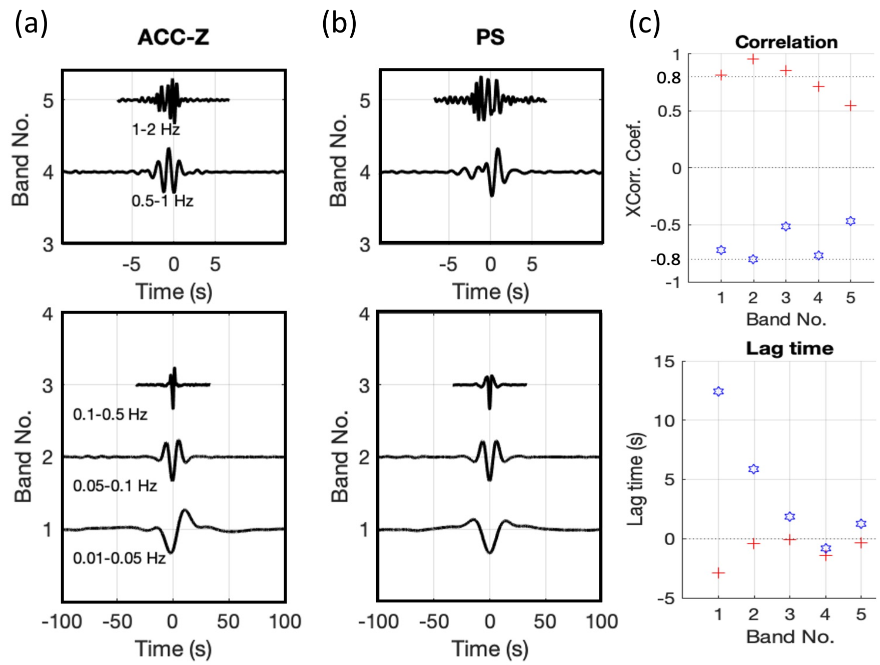

Figure 7. An example of the filter bank of (a) the vertical acceleration data and (b) the resampled pressure data. The waveforms filtered at Band 1 – Band 3 are shown in the bottom panel and those filtered at Band 4 – Band 5 are displayed in the top panel. The horizontal axis shows the time centered at the encounter of a convective vortex. (c) The maximum and minimum correlation coefficients (top panel) and the lag time (bottom panel) at each frequency band.

4.4 Asymmetricity of pressure drop profiles

Looking at the pressure data, we often observe asymmetric pressure drop profiles. According to Lorenz et al. (2021), these features might be related to non-uniform vortex wall structures. However, a solid conclusion to this problem has yet to be obtained. To better understand the relationship between the asymmetricity and the vortex structures, we start by quantitatively evaluating the symmetricity of the pressure drop profile.

In this study, we defined the asymmetricity (R_{asy}) using the integral values of the left- and right-side profiles from the maximum pressure drop time. The actual process was as follows. First, we smoothed the 20 min-long detrended PS data with a 1 s time window (Figure 8a). Second, we divided the pressure profile into the left and right sides at the time offset parameter μ. Then, we fitted each side profile with a Half-Gaussian profile (f_{GH}) defined as:

$$f_{\mathrm{GH}}(t) = \begin{cases} \frac{A}{\sqrt{2\pi}} \exp\left[-\frac{(t-\mu)^2}{2\sigma_1^2}\right] & (t < \mu), \\ \\ \frac{A}{\sqrt{2\pi}} \exp\left[-\frac{(t-\mu)^2}{2\sigma_2^2}\right] & (t \geq \mu), \end{cases} \tag{4}$$

where A is a constant, t is time, σ_1 and σ_2 correspond to the half-maximum width for the left- and right-hand profiles, respectively. The event duration t_{eff} is defined as:

$$t_{\mathrm{eff}} = \sigma_1 + \sigma_2. \tag{5}$$

Figure 8b shows an example of the best fit. Finally, the integral of both sides was performed within the time interval of $-6\sigma_1 \leq t - \mu \leq 0$ for the left side (S_L) and $0 \leq t - \mu \leq 6\sigma_2$ for the right side (S_R) (Figure 8c). The asymmetricity (R_{asy}) can be defined with the integral values as:

$$R_{\mathrm{asy}} = \log_{10}\left(\frac{S_R}{S_L}\right). \tag{6}$$

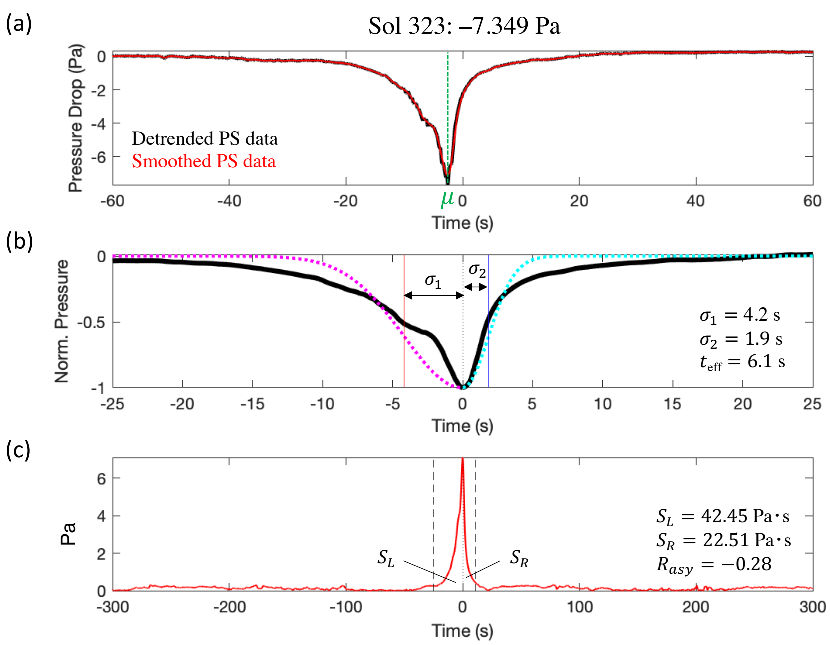

Figure 8. (a) Pressure drop signal observed on Sol 323. The black profile is the detrended pressure data, and the red is the smoothed data with a 1 s time window. μ is the time offset parameter in Equation 4. (b) Gaussian fitting results. The black profile shows the smoothed pressure data, which is time-shifted by μ for visualization. Note that the profile is normalized by the maximum value of the absolute amplitude. The magenta and the cyan dotted lines are the Gaussian profile used for fitting the left- and right-hand profiles, respectively. (c) Pressure drop profile used for the calculation of integral values. The red curve is the pressure drop profile smoothed and converted into absolute value. The dotted vertical lines show the time interval for the integral, which is set to $6\sigma_1$ and $6\sigma_2$ from the center for the left and right sides, respectively.

The histogram of the asymmetricity is presented in Figure 9a, where R_{asy}=0 means completely symmetric. Figure 9b shows a few examples of different asymmetric profiles.

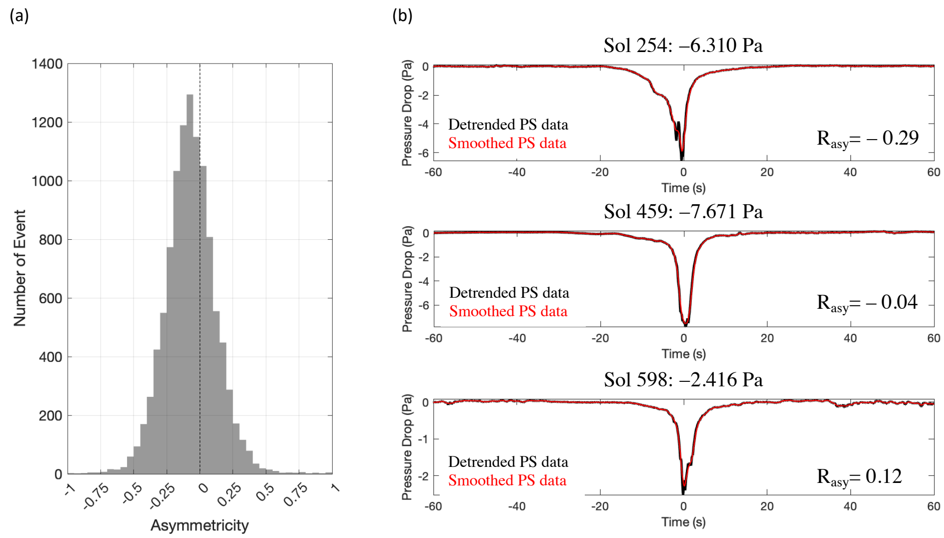

Figure 9. (a) Histogram of the asymmetricity. (b) Examples of pressure drop profiles for the cases of negative asymmetric ($R_{\mathrm{asy}} < 0$), symmetric ($R_{\mathrm{asy}} \sim 0$), and positive asymmetric ($R_{\mathrm{asy}} > 0$) from top to bottom.

Here, we call the "negative" asymmetric profile when R_{asy} <0 and the "positive"" asymmetric profile when R_{asy} >0. The histogram shows that the population reaches the peak around $R_{\mathrm{asy}} = -0.1$, indicating the majority of events are negatively asymmetric as shown in the top panel in Figure 9b. A short discussion on this result and the relation with other parameters can be found in Section 5.1.

The evaluated parameters from Section 4.1 to Section 4.4 are compiled as a binary catalog (Onodera, 2023a). The explanation of the catalog format is summarized in Appendix A.

5 Contribution to scientific investigations

In this section, we demonstrate how our catalog can contribute to deepening our understanding of the Martian environment. Here we focus on two topics. One is dedicated to the meteorological interpretations of a vortex structure implied from asymmetric features seen in pressure drop profiles (Section 5.1), and the other is related to the interaction between the atmosphere and the ground, which is useful for subsurface rigidity assessments (Section 5.2).

5.1 Interpretating the asymmetrical feature of pressure drop profiles

5.1.1 Relation between asymmetricity and the vortex structures

As presented in Figure 9, we found that the majority of pressure drop events showed the negatively asymmetric feature (i.e., a gradual drop toward the maximum pressure drop and a rapid recovery after the encounter), which is consistent with the result by Lorenz et al. (2021) who also quantified the asymmetricity using the large pressure drops (> 0.8 Pa). This result may look unreasonable in considering the two-dimensional space, where a vortex circle moves with a constant advection speed (driven by the ambient winds). In this case, a symmetric pressure drop should always be observed at the encounter with a station. Introducing a fluctuation in the advection speed could produce asymmetric profiles. However, in such a case, the population of asymmetricity would be random because we do not imagine that the advection speed changes in the same way for every event. Additionally, since the InSight landing site is located at a relatively flat area (e.g., Golombek et al., 2020), we do not expect a specific geological feature to contribute to the skewed distribution of the pressure drop asymmetricity.

When considering the three-dimensional system, a convective vortex (whirlwind) or dust devil can be modeled with a cylinder, where the wind speed may vary with altitude (e.g., Sinclair, 1973; Lorenz et al., 2021). As speculated by Lorenz et al. (2021), when the ambient wind speed at the ground c_{grd} coincides with that at the upper part of a vortex cylinder c_{up} ($c_{grd} = c_{up}$), a symmetric pressure drop would be observed at the encounter. In the case of $c_{grd} < c_{up}$, the cylinder would be tilted in the direction of advection, resulting in a "negative" asymmetric profile. On the contrary, for $c_{grd} > c_{up}$, the cylinder should be tilted in the direction opposite to the advection direction, leading to a "positive" asymmetricity. Generally speaking, the wind speed increases with altitude because the surface friction has less influence on the wind behavior at higher altitudes (e.g., Spiga et al., 2021). Additionally, the dynamic pressure is proportional to the square of wind speed. As the observations of dust devils in the terrestrial field support this idea (Sinclair, 1973), our qualitative interpretation of a skewed distribution in Figure 9a seems plausible. Further detailed discussion is out of the scope of this study; however, combining our results with some numerical experiments and/or comparing the terrestrial observations would help to illustrate the vortex structure better.

5.1.2 Relation between asymmetricity and ground coupling

Atmosphere-ground interaction is an important aspect of a convective vortex (i.e., a moving low-pressure system) because it allows us to estimate the subsurface physical properties (Section 5.2). The quality of the coupling is usually assessed with the cross-correlation between the ground motion and the pressure variation. Through the investigation of the relations between the parameters we cataloged, we found some interesting features when making a plot of asymmetricity against the cross-correlation coefficient (CC). Here, we summarize them and introduce a question for future studies.

Figure 10 shows the scatter plots of the asymmetricity and CC for different frequency bands (Band 1 – Band 5). Normally, we refer to events with CC ≥ 0.8 as "high-correlation events". As a general characteristic, the number of high-correlation events decreases as the frequency increases because they are more easily contaminated by background noises, such as wind turbulence, at a high frequency (> 1 Hz). Another notable point is that a higher correlation coefficient is obtained as the asymmetricity decreases (e.g., in Bands 2 and 3 in Figure 10). This implies that a better ground coupling occurs when a pressure drop is asymmetric rather than in the ideal symmetric case. However, it has yet to be understood whether "negative" asymmetricity is a necessary condition to increase atmosphere-ground coupling. This would be an interesting area for future work in order to better illustrate how the atmosphere and the ground interact with each other.

In addition to the above discussions, when comparing the low-frequency bands (Band 1 – Band 3), it appears that Band 1 shows a different distribution to the other bands. It is clear that the number of high-correlation events is smaller than those of Band 2 and Band 3. We suspect that the efficiency and/or quality of the atmosphere-ground coupling changes below 0.05 Hz, which could correspond to a critical point below which the ground does not deform efficiently against an external force. Or, there may be other signals dominating at the lower frequencies. This point is briefly discussed in Section 5.2.5 although we could not reach a satisfactory explanation thus far.

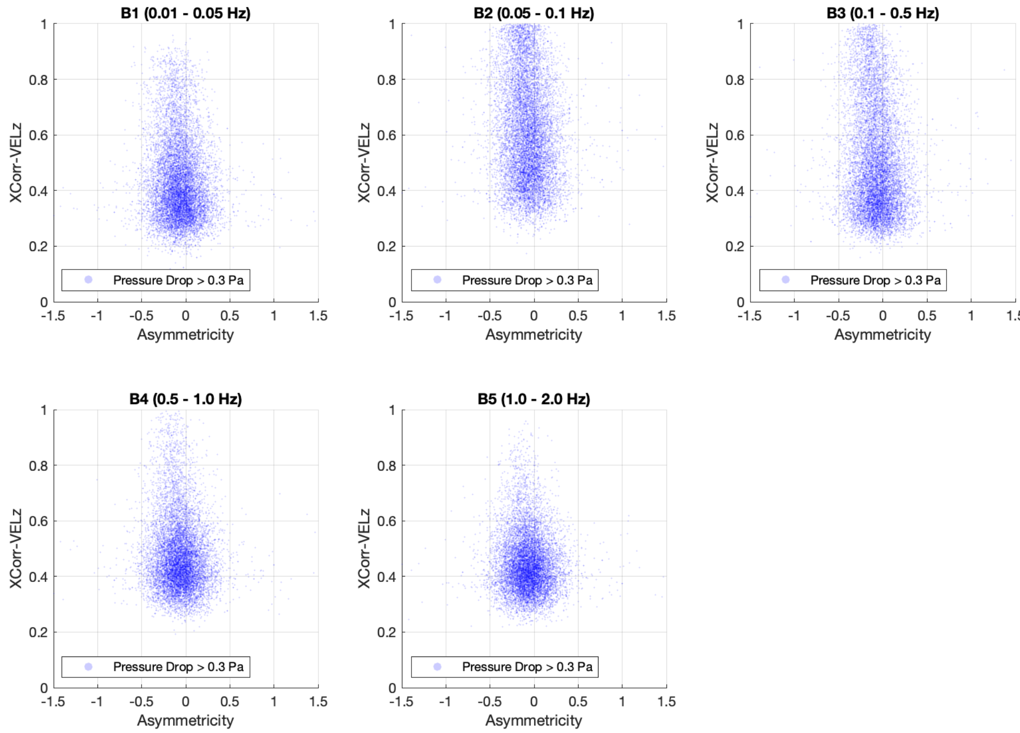

Figure 10. Scatter plots of cross-correlation coefficient against asymmetricity between the vertical ground velocity and the pressure data at five frequency bands.

5.2 Compliance analysis and 1D rigidity structure at the InSight landing site

5.2.1 Fundamental idea of compliance analysis

As briefly mentioned in Section 4.3, Sorrells (1971) formulated the relation between pressure load and vertical ground velocity for a homogeneous half-space structure as Equation 3 through the seismic and meteorological observations on Earth. The compliance can be defined by taking the spectral ratio between the ground velocity and pressure:

$$\begin{aligned} \kappa_v &= \frac{|v_z(\omega)|}{|-iP(\omega)|} = 2c\frac{1-\nu^2}{E}, \\ \kappa_h &= \frac{|v_h(\omega)|}{|P(\omega)|} = c\frac{(1+\nu)(1-2\nu)}{E}, \end{aligned} \tag{7}$$

where κ_v and κ_h are called vertical compliance and horizontal compliance, respectively. The basic idea is to retrieve the subsurface rigidity structure by inverting the compliance profile. In this study, following Kenda et al. (2020), we use the normalized compliance ($\overline{\kappa_v}$ and $\overline{\kappa_h}$) defined as follows:

$$\begin{aligned} \overline{\kappa_v} &= 2\frac{1-\nu^2}{E}, \\ \overline{\kappa_h} &= \frac{(1+\nu)(1-2\nu)}{E}. \end{aligned} \tag{8}$$

In the case of the horizontal component, there is an apparent effect (i.e., tilt effect) caused by the ground deformation. Generally, it is difficult to distinguish the horizontal compliance from the tilt effect without tracking the vortex trajectory. Here, we focus on the vertical component in the subsequent analysis.

It is worth noting that Equations 8 are valid only for a homogeneous half-space structure. When considering a potential stratified half space like this study, one can use the Thomson-Haskell propagator method (Thomson, 1950; Haskell, 1953) as demonstrated in Sorrells and Goforth (1973) and Kenda et al. (2020).

In solving the inversion problem, we employed almost the same approach performed by Kenda et al. (2020) — Bayesian inversion based on the Markov chain Monte Carlo (McMC) algorithm. The main differences from their analysis are: (i) the dataset covering the full observation period is used, and (ii) the inversions were conducted for different wind speed groups, which allows us to retrieve different depth information. As for the first point, while Kenda et al. (2020) had analyzed the data up to Sol 227, we used the data up to Sol 900, which increased the number of available events for analysis by a factor of 10. Regarding the second point, assuming the vortices are transported by the ambient wind c, we divided the two groups based on the histogram shown in Figure 5b — WS1 (3.8 m/s $< c \leq$ 8.5 m/s) and WS2 (8.5 m/s $< c <$ 16 m/s). Since c is related to the spatial resolution (or wavelength) in the compliance analysis, different compliance profiles can be obtained depending on the value of c for a certain rigidity structure model. Figure 11 gives an example, where the cases of $c =$5 m/s and 12 m/s are compared. Looking at the theoretical curves in Figure 11b, a smaller c value returns a higher normalized compliance, meaning that a smaller c is more sensitive to the shallower sub-surface structure. Thus, in the following inversion, we try to retrieve different depth information by analyzing WS1 and WS2 separately.

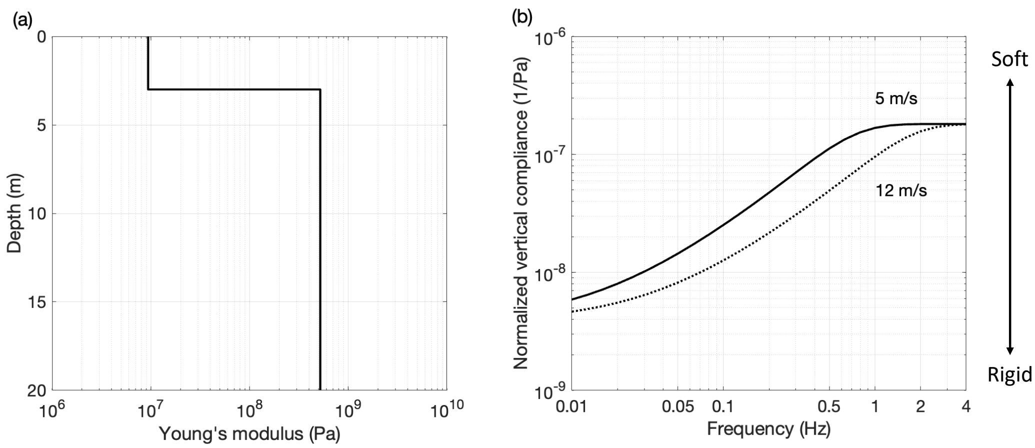

Figure 11. (a) Rigidity structure model for a demonstration. (b) Synthetic vertical compliance for different advection speeds (i.e., ambient wind speeds). The compliance is normalized by each advection speed, normally called normalized compliance. The solid line shows the compliance for the case of ambient wind speed of 5 m/s, and the dotted line does that for the 12 m/s case.

5.2.2 Data selection

Sorrells' theory is applicable only when the ground is well coupled with the atmosphere. In order to select such events, we referred to the cross-correlation coefficients (CC) calculated in Section 4.3. For the five frequency bands defined in Section 4.1, we extracted high-correlation events (CC $\geq$ 0.8) and made a 2-D probability density map of the normalized vertical compliance for WS1 and WS2, respectively (Figures 12a-b).

In this study, we paid particular attention to Band 2 and Band 3 — a similar frequency band used by Kenda et al. (2020) (0.02 – 0.3 Hz) — because of the number of events showing high CC (several hundred) and the high probability (~ 30 %).

5.2.3 Bayesian inversion

For the inversions, we took the median of the compliance profiles for Band 2 and Band 3 and smoothed them over 10 data points. The error range was evaluated with the standard deviation of all the selected compliance profiles. In Figures 12c-d, the thick black profiles correspond to the median profiles, and the thin curves illustrate the error range for WS1 and WS2, respectively.

In the inverse problem, the vertically varying structures of Young's modulus and Poisson's ratio are retrieved by fitting the observed compliance profiles (Figures 12c-d). Since this problem is ill-posed, various structure models can match the observation within its error range; in other words, we cannot determine the structure uniquely. Thus, we employed a Bayesian approach to statistically assess the resultant structure and its uncertainty. Following Kenda et al. (2020), the inversion was carried out with a Markov chain Monte Carlo (McMC) method (e.g., Mosegaard & Tarantola, 1995; Tarantola, 2004). Because this approach has been applied to other InSight-related works (e.g., Banerdt et al., 2020; Lognonné et al., 2020) and described by Kenda et al. (2020), here we only explain the main points.

The structures that fit the observations within the error range were searched out of prior distribution. The prior distribution defines a possible parameter range for the varying parameters, allowing us to get the physically possible solutions. Following Kenda et al. (2020), for 8 layers structure model, the layer's thickness, Young's modulus, and Poisson's ratio were varied in the range of 0 – 200 m, 10^6 – 10^{12} Pa, and 0.05 – 0.45, respectively. For every calculation step, the synthetic normalized compliance was computed for a given structure model within the prior distribution, then we evaluated misfit (L) defined as:

$$L = \sum_{N} \frac{|\log_{10} C^{obs} - \log_{10} C^{calc}|}{\log_{10} \sigma}, \tag{9}$$

where C^{obs} is the observed normalized compliance, C^{calc} is the synthetic normalized compliance, and σ is the uncertainty of the observation. N refers to the grid number in the frequency domain. To get a robust result (i.e., to minimize the influence of outliers), the misfit was evaluated on a logarithmic scale. Once a model is accepted (i.e., the synthetic curve fits the observation within the error range), other structure models are tried by giving fluctuations to the previously accepted model. Additionally, to avoid the local minima, after providing some fluctuations, the input structure model is forced to vary randomly so that we can search for all possible solutions. In the end, we obtain the acceptable structure models for WS1 and WS2 as probability distributions as shown in Figures 12e-f. The corresponding synthetic compliance profiles are shown as the color map in Figures 12c-d. Since the Poisson ratio does not greatly impact the compliance curve (Kenda et al., 2020), we mainly focus on Young's modulus in the following section.

5.2.4 Estimated subsurface rigidity at the InSight landing site

The posterior probability distributions of Young's modulus for different wind speed groups are displayed in Figures 12e-f. Both results suggest that the InSight landing site is composed of two layers. The first layer has Young's modulus of $(0.5 - 2) \times 10^8$ Pa with 5 - 20 m thickness and the second layer has Young's modulus of $(0.3-2)\times 10^9$ Pa. According to previous works (e.g., Delage et al., 2017; Golombek et al., 2017; Morgan et al., 2018), Young's modulus of regolith is in the order of 10^7 Pa in magnitude, coarse ejecta layer takes the value of around 10^8 Pa, and fractured bedrock shows 10^{10} Pa. Comparing these values, the first layer we identified corresponds to the coarse ejecta and the

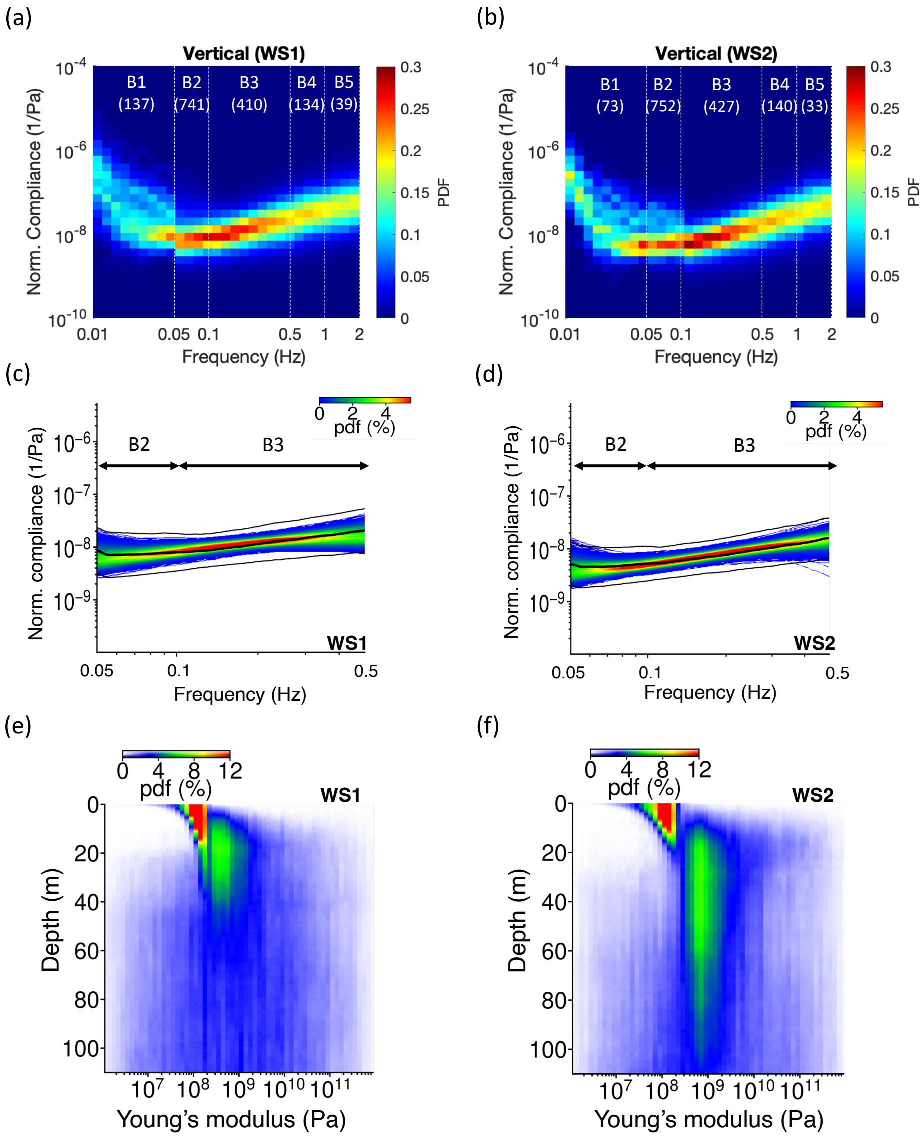

Figure 12. (a)-(b) The observed "normalized vertical compliance" for WS1 and WS2, respectively. The horizontal axis shows frequency and the vertical shows the compliance normalized with ambient wind speed. The color map represents the probability density. The hotter color indicates a higher probability. White texts at the top denote the corresponding frequency bands and the number of events used for making the probability density map. (c)-(d) Bayesian inversion results using Band 2 and Band 3 for WS1 and WS2. The horizontal axis shows frequency and the vertical axis shows the normalized compliance. The thick black lines are the median of the probability density map shown in (a) and (b), and the thin black lines display the standard deviation of the probability density map shown in (a) and (b). The color map indicates the probability density distribution of the fitting of the theoretical curve to the observation, which is linked to (e) and (f). (e)-(f) The probability density of the subsurface rigidity structure obtained through the inversion for WS1 and WS2, respectively. The horizontal axis shows Young's modulus and the vertical axis shows the depth. The hotter color indicates a higher probability.

second corresponds to more consolidated materials. Because InSight landed on the degraded crater filled with fine sand, the relatively low Young's value is expected. Our results seem consistent with the general observations at the landing site. In fact, Kenda et al. (2020), who performed a compliance analysis, also obtained a similar structure to ours down to 20 m depth.

The difference between WS1 and WS2 can be found at (i) the transition depth from the first layer to the second layer and (ii) the depth extent of the second layer. Regarding the transition depth, WS1 has a smaller wind speed, and its compliance is more sensitive to the shallower part than that of WS2. Therefore, we have a higher degree of confidence in the WS1 result and interpret that the transition from the coarse ejecta to a more consolidated layer occurs around 5 - 15 m deep, which looks consistent with the sub-surface structure model proposed by Warner et al. (2022) who constructed the subsurface structure model based on both in-situ and orbital geological observations. It is worth noting that the higher frequency contents in the compliance profile also help us to better resolve the shallower structure; thereby, applying Sorrells' theory to higher frequency bands such as Band 4 – 5 would be useful for further investigation. This point is discussed in Section 5.2.5.

Concerning the deeper part, WS2 is more sensitive than WS1, and we consider that the second layer can extend down to 100 m depth. Together with the above discussion, the subsurface rigidity structure at the InSight landing site can be modeled with two layers. The structure consists of the coarse ejecta down to 5 – 15 m depth and gets more consolidated below that depth, extending down to 100 m. Although a previous seismological study (e.g., Hobiger et al., 2021) indicates the presence of a low rigidity layer ($\sim 10^7$ Pa) at 30 – 75 m, there is no strong evidence of such a layer at the corresponding depth (30 – 75 m) around the InSight landing site or Elysium Planitia from either geological observations or compliance analyses (e.g., Warner et al., 2022; Kenda et al., 2020). Looking at Figure 12f, while a higher probability is obtained around 10^9 Pa at a depth of 30 – 75 m, some low rigidity values ($\sim 10^7$ Pa) seem acceptable (bluish area). However, the model including such low rigidity values at 30 – 75 m returns the compliance away from the median profile of the observation (compare blue profiles and thick black line in Figure 12d). Therefore, like Warner et al. (2022) and Kenda et al. (2020), our results prefer simpler structure and do not positively support the presence of a low rigidity layer indicated by some seismological analyses (e.g., Hobiger et al., 2021).

5.2.5 Implications for further extension of compliance analysis

For further extension of the compliance approach, we summarize some ideas in this section for the following studies. Going back to Figures 12a-b, we found that Band 1 shows significantly different behavior compared to the others. Considering that an unreasonably low-rigidity layer ($\sim 10^6$ Pa) shows up at several tens of meters deep if we include Band 1 in the inversion (Figure B1), Sorrells' theory might not be applicable to this frequency band. In fact, since Sorrells (1971) assumes a plane wave for compliance analysis, the theory may not work at the lower frequency where the influence of the vortex curvature gets dominant. As another possibility, as seen on Earth, the Newtonian attraction related to the pressure perturbations could affect the seismic observations (Van Camp et al., 2017; Zürn & Wielandt, 2007). However, we found that its effect was much smaller (ten times at least) than the ground compliance at 0.01 – 0.05 Hz (Appendix C and Figure C1). Thus, so far, we have not yet found a reasonable explanation for the compliance behavior in Band 1. Given these indications, one should avoid using Band 1 until the physical mechanism at the very low frequency (< 0.05 Hz) is figured out. In our future work, the applicability of Sorrells' theory to the very low frequency (< 0.05 Hz) will be discussed.

On the other hand, it might be possible to apply Sorrells' theory to higher frequencies (> 0.5 Hz). Unlike Band 1, the probability density of compliance in Bands 4 and 5 is as stable as in Bands 2 and 3, and shows good continuity between each band. We think these events are helpful in resolving the shallow structures better even though there are a smaller number of events compared to Band 2 and 3. We guess the reason for their smaller population is that they are relatively small convective vortices. Smaller vortices are more easily affected by local turbulence and gain more noise, decreasing the correlation between pressure variations and ground motions. This leads to a smaller number of events available for compliance analysis. However, once a vortex structure becomes stable enough against shear forces by turbulence and is close enough to an observation point, a better atmosphere-ground coupling can be observed. To test our hypothesis, we will look closer at the higher frequency part — which can help us extract the uppermost structures (a few meter depth).

6 Concluding remarks

For the purpose of providing useful information for the studies on the Martian atmosphere and subsurface structures, we quantitatively characterized 12,569 convective vortices observed by InSight from both meteorological and seismological aspects. The evaluated parameters (e.g., event time, pressure deficit, event duration, asymmetricity, and cross-correlation coefficient between pressure variation and ground motion) are compiled as a catalog that is available online (Onodera, 2023a).

As examples of scientific application, we investigated the asymmetricity of pressure drop profiles. Some discussions led to the idea that asymmetricity is related to the vortex wall structure rather than a two-dimensional advection pattern. We expect future studies will investigate our hypothesis through numerical experiments. Additionally, using events that show a high correlation between pressure and seismic (ground motion) data, we performed a compliance analysis and estimated the subsurface rigidity at the InSight landing site down to a depth of ~ 100 m. Our results suggest that the subsurface structure can be modeled with two layers: a coarse ejecta layer ($\sim 10^8$ Pa) and a more consolidated layer ($\sim 10^9$ Pa). It is indicated that the transition from the first layer to the second occurs at $5 - 15$ m depth, which is consistent with previously proposed models (e.g., Kenda et al., 2020; Warner et al., 2022). It is worth noting that this value could be refined by including the high-frequency content in the compliance analysis because it is more sensitive to shallower depths (< 5 m).

Together with some results and discussions in this paper, this catalog will help improve our knowledge of the Martian convective vortices as well as atmosphere-ground interaction.

Appendix A Catalog format

All the previously presented data and parameters are gathered in a catalog. The catalog is available in pickle format — a binary format produced by pandas module of python — at Onodera (2023a). To read a pickle file, readers may try the following lines:

```
import pandas as pd
data = pd.read_pickle("path to pickle file")
```

By choosing the parameter name listed in Table A1 and A2, readers can retrieve parameters depending on their interests. For example, one can get the list of all pressure drop values by running the line below:

```
param=data.PressD
```

Table A1. List of parameter names related to event ID, detection time, pressure drop values, ambient factors, and signal-to-noise ratio in our catalog.

Name	Unit	Description	References
ID	-	The number is allocated from the largest pressure drop event to the smaller ones.	Spiga et al. (2021)
Sol	-	InSight sol (Martian day)	Spiga et al. (2021)
LTST_h	hour	Local True Solar Time in hours at the maximum pressure drop	Spiga et al. (2021)
UTC	YYYY-DOYThh:mmm:ss	Corresponding UTC of LTST_h	Spiga et al. (2021)
PressD	Pa	Value of the minimum pressure during the encounter of a vortex	Spiga et al. (2021)
Ave_WS	m/s	Average wind speed	Section 4.2
std_WS	m/s	Standard deviation of wind speed	Section 4.2
Ave_Wdir	N°E	Average wind direction	Section 4.2
std_Wdir	N°E	Standard deviation of wind direction	Section 4.2
Ave_AT	K	Average air temperature	Section 4.2
std_AT	K	Standard deviation of air temperature	Section 4.2
SNR_ACCZ_BX	-	The signal-to-noise ratio of the vertical acceleration recorded by VBB at Band X (X = 1,2,...,5)	Section 4.1
SNR_ACCN_BX	-	The signal-to-noise ratio of the north acceleration recorded by VBB at Band X (X = 1,2,...,5)	Section 4.1
SNR_ACCE_BX	-	The signal-to-noise ratio of the east acceleration recorded by VBB at Band X (X = 1,2,...,5)	Section 4.1
SNR_PS_BX	-	The signal-to-noise ratio of the pressure signal recorded by PS at Band X (X = 1,2,...,5)	Section 4.1

565 # Appendix B Additional Inversion Result

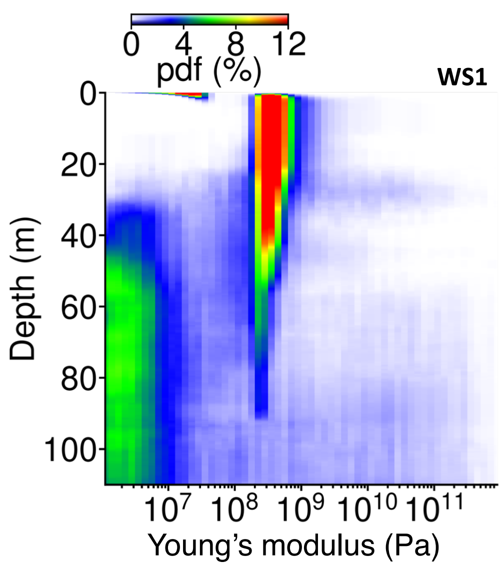

Figure B1. Probability density map for Young's modulus derived through compliance analysis (WS1) taking into account all frequency bands. There is an unreasonably soft layer ($< 5 \times 10^6$ Pa) below 45 m depth which is closely related to Band 1.

Table A2. List of parameter names related to cross-correlation and asymmetricity in our catalog.

Name	Unit	Description	References
XCC_max_VELZ_BX	-	The maximum value of the cross-correlation coefficient between the vertical velocity (VBB-Z) and phase-shifted pressure data (PS) at Band X (X = 1,2,...,5)	Section 4.3
XCC_max_VELN_BX	-	The maximum value of the cross-correlation coefficient between the north velocity (VBB-N) and pressure data (PS) at Band X (X = 1,2,...,5)	Section 4.3
XCC_max_VELE_BX	-	The maximum value of the cross-correlation coefficient between the east velocity (VBB-N) and pressure data (PS) at Band X (X = 1,2,...,5)	Section 4.3
XCC_min_VELZ_BX	-	The minimum value of the cross-correlation coefficient between the vertical velocity (VBB-Z) and phase-shifted pressure data (PS) at Band X (X = 1,2,...,5)	Section 4.3
XCC_min_VELN_BX	-	The minimum value of the cross-correlation coefficient between the north velocity (VBB-N) and pressure data (PS) at Band X (X = 1,2,...,5)	Section 4.3
XCC_min_VELE_BX	-	The minimum value of the cross-correlation coefficient between the east velocity (VBB-N) and pressure data (PS) at Band X (X = 1,2,...,5)	Section 4.3
XCC_max_ACCZ_BX	-	The maximum value of the cross-correlation coefficient between the vertical acceleration (VBB-Z) and pressure data (PS) at Band X (X = 1,2,...,5)	Section 4.3
XCC_max_ACCN_BX	-	The maximum value of the cross-correlation coefficient between the north acceleration (VBB-N) and phase-shifted pressure data (PS) at Band X (X = 1,2,...,5)	Section 4.3
XCC_max_ACCE_BX	-	The maximum value of the cross-correlation coefficient between the east acceleration (VBB-E) and phase-shifted pressure data (PS) at Band X (X = 1,2,...,5)	Section 4.3
XCC_min_ACCZ_BX	-	The minimum value of the cross-correlation coefficient between the vertical acceleration (VBB-Z) and pressure data (PS) at Band X (X = 1,2,...,5)	Section 4.3
XCC_min_ACCN_BX	-	The minimum value of the cross-correlation coefficient between the north acceleration (VBB-N) and phase-shifted pressure data (PS) at Band X (X = 1,2,...,5)	Section 4.3
XCC_min_ACCE_BX	-	The minimum value of the cross-correlation coefficient between the east acceleration (VBB-E) and phase-shifted pressure data (PS) at Band X (X = 1,2,...,5)	Section 4.3
t_lag_max_VELZ_BX	-	The lag time for "XCC_max_VELZ_BX" (X=1,2,. . . ,5)	Section 4.3
t_lag_max_VELN_BX	-	The lag time for "XCC_max_VELN_BX" (X=1,2,. . . ,5)	Section 4.3
t_lag_max_VELE_BX	-	The lag time for "XCC_max_VELE_BX" (X=1,2,. . . ,5)	Section 4.3
t_lag_min_VELZ_BX	-	The lag time for "XCC_min_VELZ_BX" (X=1,2,. . . ,5)	Section 4.3
t_lag_min_VELN_BX	-	The lag time for "XCC_min_VELN_BX" (X=1,2,. . . ,5)	Section 4.3
t_lag_min_VELE_BX	-	The lag time for "XCC_min_VELE_BX" (X=1,2,. . . ,5)	Section 4.3
t_lag_max_ACCZ_BX	-	The lag time for "XCC_max_ACCZ_BX" (X=1,2,. . . ,5)	Section 4.3
t_lag_max_ACCN_BX	-	The lag time for "XCC_max_ACCN_BX" (X=1,2,. . . ,5)	Section 4.3
t_lag_max_ACCE_BX	-	The lag time for "XCC_max_ACCE_BX" (X=1,2,. . . ,5)	Section 4.3
t_lag_min_ACCZ_BX	-	The lag time for "XCC_min_ACCZ_BX" (X=1,2,. . . ,5)	Section 4.3
t_lag_min_ACCN_BX	-	The lag time for "XCC_min_ACCN_BX" (X=1,2,. . . ,5)	Section 4.3
t_lag_min_ACCE_BX	-	The lag time for "XCC_min_ACCE_BX" (X=1,2,. . . ,5)	Section 4.3
STDEV1	sec	The standard deviation of the fitted pressure drop with the left-hand side Gaussian fit	Section 4.4
STDEV2	sec	The standard deviation of the fitted pressure drop with the right-hand side Gaussian fit	Section 4.4
T_eff_s	sec	Effective event time (i.e., the characteristic time scale of event duration), defined by STDEV1 + STDEV2	Section 4.4
Residual_GaussFit	Pa	Summation of the residual value when PS was fitted with Gaussian curve	Section 4.4
Int1	Pa·s	The integral value of the left-hand side of the pressure drop signal	Section 4.4
Int2	Pa·s	The integral value of the right-hand side of the pressure drop signal	Section 4.4
Asymmetricity	-	The asymmetricity of pressure drop, defined as log10(Int2/Int1)	Section 4.4

Appendix C Effect of Newtonian Attraction

It is well known that seismic observations are influenced by changes in environmental factors, one of which is the atmospheric conditions as described in this study. While this study focused on the ground deformation caused by transient pressure variations, there is another effect relevant to a change in atmospheric conditions. For example, when the air above the observation point is denser than the surrounding air, the sensor mass would be attracted toward the denser part (i.e., Newtonian attraction). According to Zürn and Wielandt (2007), the effect of Newtonian attraction becomes dominant below 2 mHz on Earth, whose intensity can be evaluated as follows:

$$\frac{\Delta g}{\Delta p} = -\frac{2\pi G}{g_0}, \tag{C1}$$

where G is gravitational constant and g_0 is the gravitational acceleration (Earth: 9.81 m/s^2, Mars: 3.72 m/s^2). The terrestial value is -4.3×10^{-2}(nm/s^2/Pa) and the Martian value is -1.1×10^{-1} (nm/s^2/Pa). Figure C1 compares the absolute intensity of Newtonian attraction and that of vertical compliance. At our target frequency (> 0.01 Hz), Newtonian attraction is much smaller than the vertical compliance, leading to the conclusion that the unstable behavior at 0.01 – 0.05 Hz in Figures 12a-b cannot be explained with Newtonian attraction.

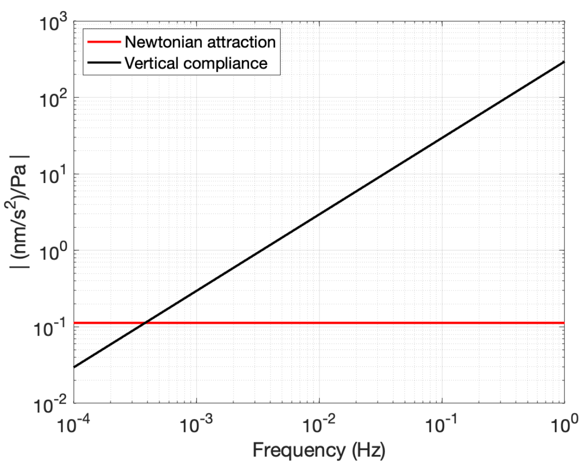

Figure C1. Comparison of the absolute intensity of Newtonian attraction and the vertical compliance. The vertical compliance was computed by multiplying 2π with Equation 7, assuming E=2×10^8 (Pa), $\nu = 0.25$, and $c = 5.0$ (m/s).

Data availability

The SEIS data from the InSight mission used in this study can be retrieved through InSight Mars SEIS Data Service (2019) and InSight Marsquake Service (2022). The catalog file is available at Onodera (2023a). A sample program for analyzing the VBB data can be found at Onodera (2023b).

Acknowledgments

We acknowledge NASA, CNES, their partner agencies and Institutions (UKSA, SSO, DLR, JPL, IPGP-CNRS, ETHZ, IC, and MPS- MPG), and the flight operations team at JPL, SISMOC, MSDS, IRIS-DMC, and PDS for acquiring and providing InSight data, including SEED SEIS data. This is InSight contribution number 326. K.O. is supported by JSPS KAKENHI Grant Number 22KJ0745. A.H. is funded by the UK Space Agency under grant numbers ST/R002096/1 and ST/W002523/1. M.D. was granted access to the GENCI HPC resources of IDRIS under allocation AD010413017R1. Numerical computations were partly performed on the S-CAPAD/DANTE platform, IPGP, France.

References

Banerdt, W. B., Smrekar, S. E., Banfield, D., Giardini, D., Golombek, M., Johnson, C. L., … Wieczorek, M. (2020). Initial results from the insight mission on mars. *Nature Geoscience*, *13*(3), 183-189. Retrieved from `https://doi.org/10.1038/s41561-020-0544-y` doi: 10.1038/s41561-020-0544-y

Banfield, D., Rodriguez-Manfredi, J. A., Russell, C. T., Rowe, K. M., Leneman, D., Lai, H. R., … Team, T. T. (2018). Insight auxiliary payload sensor suite (apss). *Space Science Reviews*, *215*(1), 4. doi: 10.1007/s11214-018-0570-x

Banfield, D., Spiga, A., Newman, C., Forget, F., Lemmon, M., Lorenz, R., … Banerdt, W. B. (2020). The atmosphere of mars as observed by insight. *Nature Geoscience*, *13*(3), 190-198. Retrieved from `https://doi.org/10.1038/s41561-020-0534-0` doi: 10.1038/s41561-020-0534-0

Bila, T., Wurm, G., Onyeagusi, F. C., & Teiser, J. (2020). Lifting grains by the transient low pressure in a martian dust devil. *Icarus*, *339*, 113569. Retrieved from `https://www.sciencedirect.com/science/article/pii/S0019103519306359` doi: https://doi.org/10.1016/j.icarus.2019.113569

Chatain, A., Spiga, A., Banfield, D., Forget, F., & Murdoch, N. (2021). Seasonal variability of the daytime and nighttime atmospheric turbulence experienced by insight on mars. *Geophysical Research Letters*, *48*(22), e2021GL095453. doi: https://doi.org/10.1029/2021GL095453

Delage, P., Karakostas, F., Dhemaied, A., Belmokhtar, M., Lognonné, P., Golombek, M., … Banerdt, B. (2017). An investigation of the mechanical properties of some martian regolith simulants with respect to the surface properties at the insight mission landing site. *Space Science Reviews*, *211*(1), 191-213. doi: 10.1007/s11214-017-0339-7

Ellehoj, M. D., Gunnlaugsson, H. P., Taylor, P. A., Kahanpää, H., Bean, K. M., Cantor, B. A., … Whiteway, J. (2010). Convective vortices and dust devils at the phoenix mars mission landing site. *Journal of Geophysical Research: Planets*, *115*(E4). Retrieved from `https://agupubs.onlinelibrary.wiley.com/doi/abs/10.1029/2009JE003413` doi: https://doi.org/10.1029/2009JE003413

Garcia, R. F., Kenda, B., Kawamura, T., Spiga, A., Murdoch, N., Lognonné, P. H., … Banerdt, W. B. (2020). Pressure effects on the seis-insight instrument, improvement of seismic records, and characterization of long period atmospheric waves from ground displacements. *Journal of Geophysical Research: Planets*, *125*(7), e2019JE006278. Retrieved from `https://agupubs.onlinelibrary.wiley.com/doi/abs/10.1029/2019JE006278` doi: https://doi.org/10.1029/2019JE006278

Giardini, D., Lognonné, P., Banerdt, W. B., Pike, W. T., Christensen, U., Ceylan, S., … Yana, C. (2020). The seismicity of mars. *Nature Geoscience*, *13*, 205-212. Retrieved from `https://doi.org/10.1038/s41561-020-0539-8` doi: 10.1038/s41561-020-0539-8

Golombek, M., Kipp, D., Warner, N., Daubar, I. J., Fergason, R., Kirk, R. L., … Banerdt, W. B. (2017). Selection of the insight landing site. *Space Science Reviews*, *211*(1), 5-95. doi: 10.1007/s11214-016-0321-9

Golombek, M., Warner, N. H., Grant, J. A., Hauber, E., Ansan, V., Weitz, C. M., … Banerdt, W. B. (2020). Geology of the insight landing site on mars. *Nature Communications*, *11*(1), 1014. doi: 10.1038/s41467-020-14679-1

Haskell, N. A. (1953). The dispersion of surface waves on multilayered media*. *Bulletin of the Seismological Society of America*, *43*(1), 17-34. doi: 10.1785/BSSA0430010017

Hobiger, M., Hallo, M., Schmelzbach, C., Stähler, S. C., Fäh, D., Giardini, D., ... Banerdt, W. B. (2021). The shallow structure of mars at the insight landing site from inversion of ambient vibrations. *Nature Communications*, *12*(1), 6756. doi: 10.1038/s41467-021-26957-7

Hueso, R., Newman, C. E., del Río-Gaztelurrutia, T., Munguira, A., Sánchez-Lavega, A., Toledo, D., ... Lepinette-Malvite, A. (2023). Convective vortices and dust devils detected and characterized by mars 2020. *Journal of Geophysical Research: Planets*, *128*(2), e2022JE007516. doi: https://doi.org/10.1029/2022JE007516

InSight Mars SEIS Data Service. (2019). *SEIS raw data, InSight mission.* IPGP, JPL, CNES, ETHZ, ICL, MPS, ISAE-Supaero, LPG, MFSC. doi: 10.18715/SEIS.INSIGHT.XB_2016

InSight Marsquake Service. (2022). *Mars Seismic Catalogue, InSight Mission; V12 2022-10-01.* ETHZ, IPGP, JPL, ICL, Univ. Bristol. doi: 10.12686/A18

Jackson, B. (2022). Vortices and dust devils as observed by the mars environmental dynamics analyzer instruments on board the mars 2020 perseverance rover. *The Planetary Science Journal*, *3*(20). doi: DOI10.3847/PSJ/ac4586

Kahanpää, H., Newman, C., Moores, J., Zorzano, M.-P., Martín-Torres, J., Navarro, S., ... Schmidt, W. (2016). Convective vortices and dust devils at the msl landing site: Annual variability. *Journal of Geophysical Research: Planets*, *121*(8), 1514-1549. doi: https://doi.org/10.1002/2016JE005027

Kenda, B., Drilleau, M., Garcia, R. F., Kawamura, T., Murdoch, N., Compaire, N., ... Spohn, T. (2020). Subsurface structure at the insight landing site from compliance measurements by seismic and meteorological experiments. *Journal of Geophysical Research: Planets*, *125*(6), e2020JE006387. Retrieved from `https://agupubs.onlinelibrary.wiley.com/doi/abs/10.1029/2020JE006387` (e2020JE006387 10.1029/2020JE006387) doi: https://doi.org/10.1029/2020JE006387

Kenda, B., Lognonné, P., Spiga, A., Kawamura, T., Kedar, S., Banerdt, W. B., ... Golombek, M. (2017). Modeling of ground deformation and shallow surface waves generated by martian dust devils and perspectives for near-surface structure inversion. *Space Science Reviews*, *211*(1), 501-524. doi: 10.1007/s11214-017-0378-0

Khan, A., Ceylan, S., van Driel, M., Giardini, D., Lognonné, P., Samuel, H., ... Banerdt, W. B. (2021). Upper mantle structure of mars from insight seismic data. *Science*, *373*(6553), 434-438. Retrieved from `https://www.science.org/doi/abs/10.1126/science.abf2966` doi: 10.1126/science.abf2966

Knapmeyer-Endrun, B., Panning, M. P., Bissig, F., Joshi, R., Khan, A., Kim, D., ... Banerdt, W. B. (2021). Thickness and structure of the martian crust from insight seismic data. *Science*, *373*(6553), 438-443. Retrieved from `https://www.science.org/doi/abs/10.1126/science.abf8966` doi: 10.1126/science.abf8966

Lognonné, P., Banerdt, W. B., Giardini, D., Pike, W. T., Christensen, U., Laudet, P., ... Wookey, J. (2019). Seis: Insight's seismic experiment for internal structure of mars. *Space Science Reviews*, *215*(1), 12. Retrieved from `https://doi.org/10.1007/s11214-018-0574-6` doi: 10.1007/s11214-018-0574-6

Lognonné, P., Banerdt, W. B., Pike, W. T., Giardini, D., Christensen, U., Garcia, R. F., ... Zweifel, P. (2020). Constraints on the shallow elastic and anelastic structure of mars from insight seismic data. *Nature Geoscience*, *13*(3), 213-220. Retrieved from `https://doi.org/10.1038/s41561-020-0536-y` doi: 10.1038/s41561-020-0536-y

Lorenz, R. D., Kedar, S., Murdoch, N., Lognonné, P., Kawamura, T., Mimoun, D.,

& Bruce Banerdt, W. (2015). Seismometer Detection of Dust Devil Vortices by Ground Tilt. *Bulletin of the Seismological Society of America*, *105*(6), 3015-3023. doi: 10.1785/0120150133

Lorenz, R. D., Spiga, A., Lognonné, P., Plasman, M., Newman, C. E., & Charalambous, C. (2021). The whirlwinds of elysium: A catalog and meteorological characteristics of "dust devil" vortices observed by insight on mars. *Icarus*, *355*, 114119. Retrieved from https://www.sciencedirect.com/science/article/pii/S0019103520304632 doi: https://doi.org/10.1016/j.icarus.2020.114119

Martínez, G. M., Newman, C. N., De Vicente-Retortillo, A., Fischer, E., Renno, N. O., Richardson, M. I., ... Vasavada, A. R. (2017). The modern near-surface martian climate: A review of in-situ meteorological data from viking to curiosity. *Space Science Reviews*, *212*(1), 295-338. Retrieved from https://doi.org/10.1007/s11214-017-0360-x doi: 10.1007/s11214-017-0360-x

Morgan, P., Grott, M., Knapmeyer-Endrun, B., Golombek, M., Delage, P., Lognonné, P., ... Kedar, S. (2018). A pre-landing assessment of regolith properties at the insight landing site. *Space Science Reviews*, *214*(6), 104. doi: 10.1007/s11214-018-0537-y

Mosegaard, K., & Tarantola, A. (1995). Monte carlo sampling of solutions to inverse problems. *Journal of Geophysical Research: Solid Earth*, *100*(B7), 12431-12447. Retrieved from https://agupubs.onlinelibrary.wiley.com/doi/abs/10.1029/94JB03097 doi: https://doi.org/10.1029/94JB03097

Murdoch, N., Kenda, B., Kawamura, T., Spiga, A., Lognonné, P., Mimoun, D., & Banerdt, W. B. (2017). Estimations of the seismic pressure noise on mars determined from large eddy simulations and demonstration of pressure decorrelation techniques for the insight mission. *Space Science Reviews*, *211*(1), 457-483. Retrieved from https://doi.org/10.1007/s11214-017-0343-y doi: 10.1007/s11214-017-0343-y

Murdoch, N., Spiga, A., Lorenz, R., Garcia, R. F., Perrin, C., Widmer-Schnidrig, R., ... Banerdt, W. B. (2021). Constraining martian regolith and vortex parameters from combined seismic and meteorological measurements. *Journal of Geophysical Research: Planets*, *126*(2), e2020JE006410. doi: https://doi.org/10.1029/2020JE006410

Murphy, J., & Nelli, S. (2002). Mars pathfinder convective vortices: Frequency of occurrence. *Geophysical Research Letters*, *29*(23), 18-1-18-4. doi: https://doi.org/10.1029/2002GL015214

Murphy, J., Steakley, K., Balme, M., Deprez, G., Esposito, F., Kahanpää, H., ... Whelley, P. (2016). Field measurements of terrestrial and martian dust devils. *Space Science Reviews*, *203*(1), 39-87. doi: 10.1007/s11214-016-0283-y

Newman, C., Bertrand, T., Battalio, J., Day, M., Juárez, M. D. L. T., Elrod, M. K., ... Zorzano, M.-P. (2021). Toward more realistic simulation and prediction of dust storms on Mars. *Bulletin of the AAS*, *53*(4). (https://baas.aas.org/pub/2021n4i278)

Newman, C., Hueso, R., Lemmon, M. T., Munguira, A., Álvaro Vicente-Retortillo, Apestigue, V., ... Guzewich, S. D. (2022). The dynamic atmospheric and aeolian environment of jezero crater, mars. *Science Advances*, *8*(21), eabn3783. doi: 10.1126/sciadv.abn3783

Onodera, K. (2023a). *InSight's seismic and meteorological data related to the Martian convective vortices.* Zenodo. doi: 10.5281/zenodo.7801343

Onodera, K. (2023b). *Sample program for analyzing the InSight seismic data.* Zenodo. doi: 10.5281/zenodo.7927454

Ordonez-Etxeberria, I., Hueso, R., & Sánchez-Lavega, A. (2018). A systematic search of sudden pressure drops on gale crater during two martian years derived from msl/rems data. *Icarus*, *299*, 308-330. doi: https://doi.org/10.1016/j.icarus.2017.07.032

Perrin, C., Rodriguez, S., Jacob, A., Lucas, A., Spiga, A., Murdoch, N., … Banerdt, W. B. (2020). Monitoring of dust devil tracks around the insight landing site, mars, and comparison with in situ atmospheric data. *Geophysical Research Letters*, *47*(10), e2020GL087234. doi: https://doi.org/10.1029/2020GL087234

Reiss, D., Spiga, A., & Erkeling, G. (2014). The horizontal motion of dust devils on mars derived from crism and ctx/hirise observations. *Icarus*, *227*, 8-20. Retrieved from https://www.sciencedirect.com/science/article/pii/S0019103513003771 doi: https://doi.org/10.1016/j.icarus.2013.08.028

Sinclair, P. C. (1973). The lower structure of dust devils. *Journal of Atmospheric Sciences*, *30*(8), 1599 - 1619. doi: https://doi.org/10.1175/1520-0469(1973)030⟨1599:TLSODD⟩2.0.CO;2

Sorrells, G. G. (1971). A Preliminary Investigation into the Relationship between Long-Period Seismic Noise and Local Fluctuations in the Atmospheric Pressure Field. *Geophysical Journal International*, *26*(1-4), 71-82. Retrieved from https://doi.org/10.1111/j.1365-246X.1971.tb03383.x doi: 10.1111/j.1365-246X.1971.tb03383.x

Sorrells, G. G., & Goforth, T. T. (1973, 10). Low-frequency earth motion generated by slowly propagating partially organized pressure fields. *Bulletin of the Seismological Society of America*, *63*(5), 1583-1601. doi: 10.1785/BSSA0630051583

Sorrells, G. G., McDonald, J. A., Der, Z. A., & Herrin, E. (1971). Earth motion caused by local atmospheric pressure changes. *Geophysical Journal of the Royal Astronomical Society*, *26*(1-4), 83-98. doi: https://doi.org/10.1111/j.1365-246X.1971.tb03384.x

Spiga, A., Banfield, D., Teanby, N. A., Forget, F., Lucas, A., Kenda, B., … Banerdt, W. B. (2018). Atmospheric science with insight. *Space Science Reviews*, *214*(7), 109. Retrieved from https://doi.org/10.1007/s11214-018-0543-0 doi: 10.1007/s11214-018-0543-0

Spiga, A., Murdoch, N., Lorenz, R., Forget, F., Newman, C., Rodriguez, S., … Banerdt, W. B. (2021). A study of daytime convective vortices and turbulence in the martian planetary boundary layer based on half-a-year of insight atmospheric measurements and large-eddy simulations. *Journal of Geophysical Research: Planets*, *126*(1), e2020JE006511. Retrieved from https://agupubs.onlinelibrary.wiley.com/doi/abs/10.1029/2020JE006511 (e2020JE006511 2020JE006511) doi: https://doi.org/10.1029/2020JE006511

Stähler, S. C., Khan, A., Banerdt, W. B., Lognonné, P., Giardini, D., Ceylan, S., … Smrekar, S. E. (2021). Seismic detection of the martian core. *Science*, *373*(6553), 443-448. Retrieved from https://www.science.org/doi/abs/10.1126/science.abi7730 doi: 10.1126/science.abi7730

Tarantola, A. (2004). *Inverse problem theory and methods for model parameter estimation.* USA: Society for Industrial and Applied Mathematics.

Thomson, W. T. (1950). Transmission of elastic waves through a stratified solid medium. *Journal of Applied Physics*, *21*(2), 89-93. doi: 10.1063/1.1699629

Van Camp, M., de Viron, O., Watlet, A., Meurers, B., Francis, O., & Caudron, C. (2017). Geophysics from terrestrial time-variable gravity measurements. *Reviews of Geophysics*, *55*(4), 938-992. doi: https://doi.org/10.1002/2017RG000566

Warner, N. H., Golombek, M. P., Ansan, V., Marteau, E., Williams, N., Grant, J. A., … Banks, M. (2022). In situ and orbital stratigraphic characterization of the insight landing site—a type example of a regolith-covered lava plain on mars. *Journal of Geophysical Research: Planets*, *127*(4), e2022JE007232. doi: https://doi.org/10.1029/2022JE007232

Zürn, W., & Wielandt, E. (2007). On the minimum of vertical seismic noise near 3 mHz. *Geophysical Journal International*, *168*(2), 647-658. doi: 10.1111/j.1365-246X.2006.03189.x

Figure1.

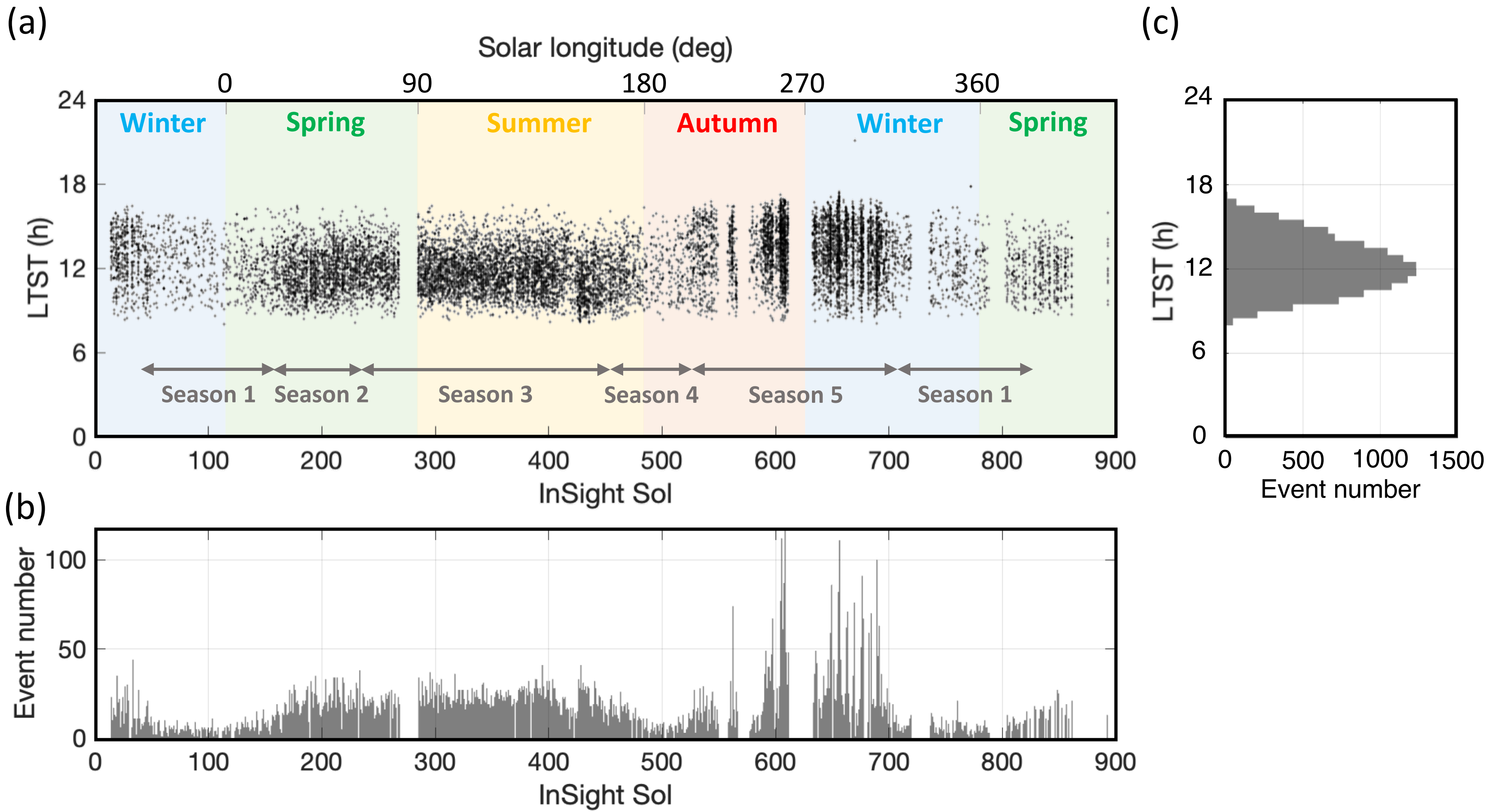
(a)
Solar longitude (deg)
0
90
180
270
360
Winter
Spring
Summer
Autumn
Winter
Spring
LTST (h)
Season 1
Season 2
Season 3
Season 4
Season 5
Season 1
InSight Sol
(b)
Event number
InSight Sol
(c)
LTST (h)
Event number

Figure2.

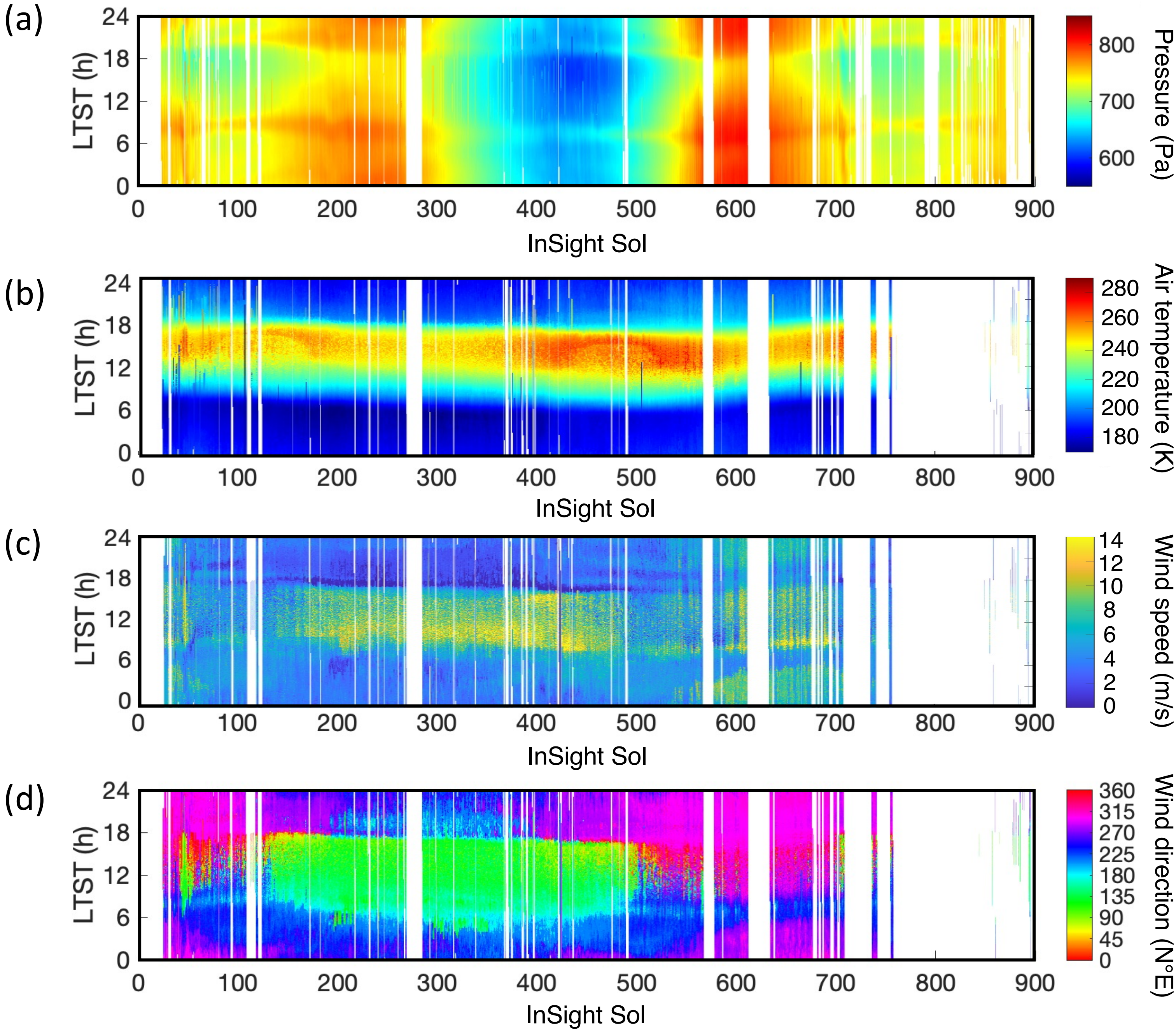

(a)
LTST (h)
InSight Sol
Pressure (Pa)
(b)
LTST (h)
InSight Sol
Air temperature (K)
(c)
LTST (h)
InSight Sol
Wind speed (m/s)
(d)
LTST (h)
InSight Sol
Wind direction (N°E)

Figure3.

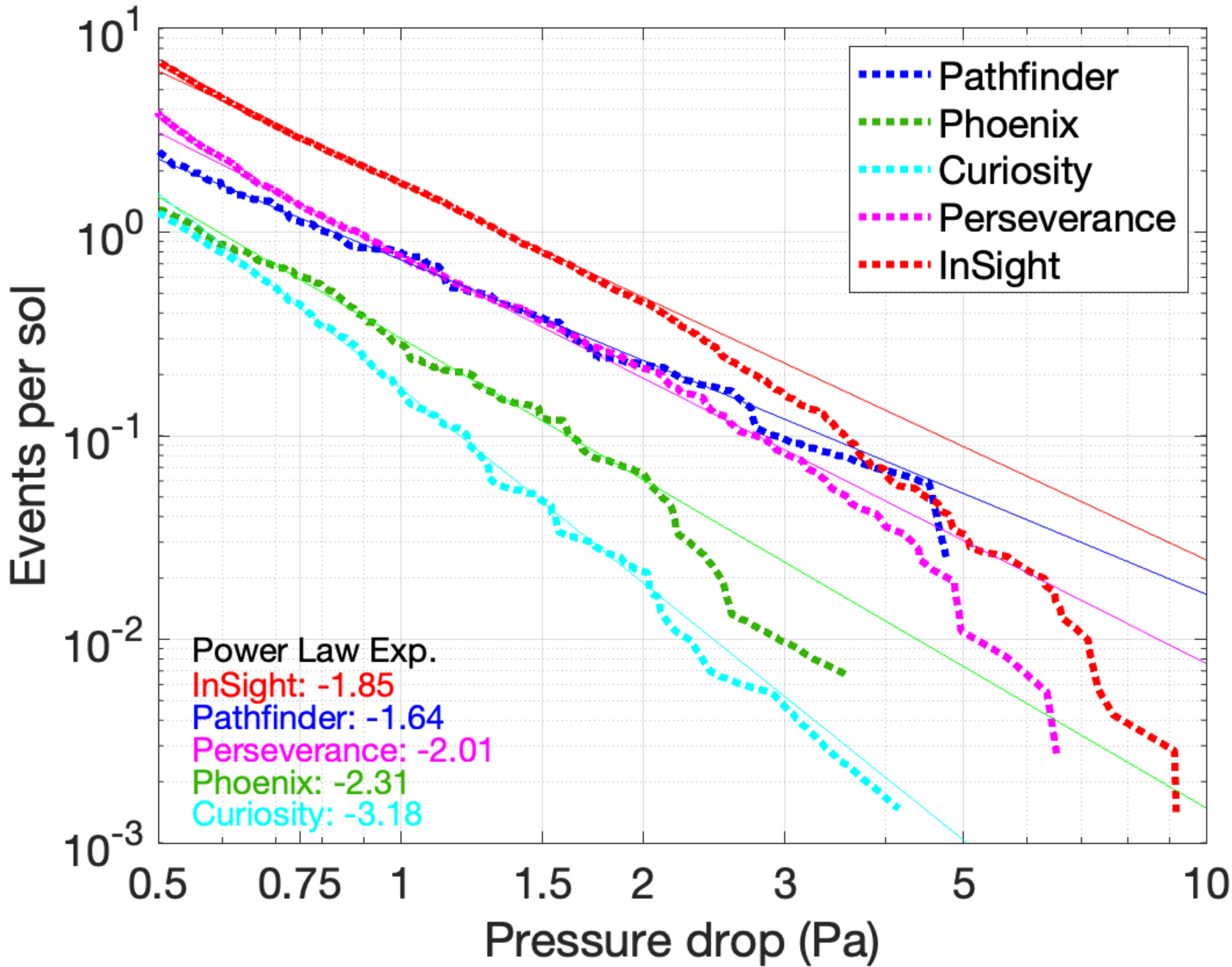

Pathfinder
Phoenix
Curiosity
Perseverance
InSight
Power Law Exp.
InSight: -1.85
Pathfinder: -1.64
Perseverance: -2.01
Phoenix: -2.31
Curiosity: -3.18
Events per sol
Pressure drop (Pa)
10^1
10^0
10^-1
10^-2
10^-3
0.5
0.75
1
1.5
2
3
5
10

Figure4.

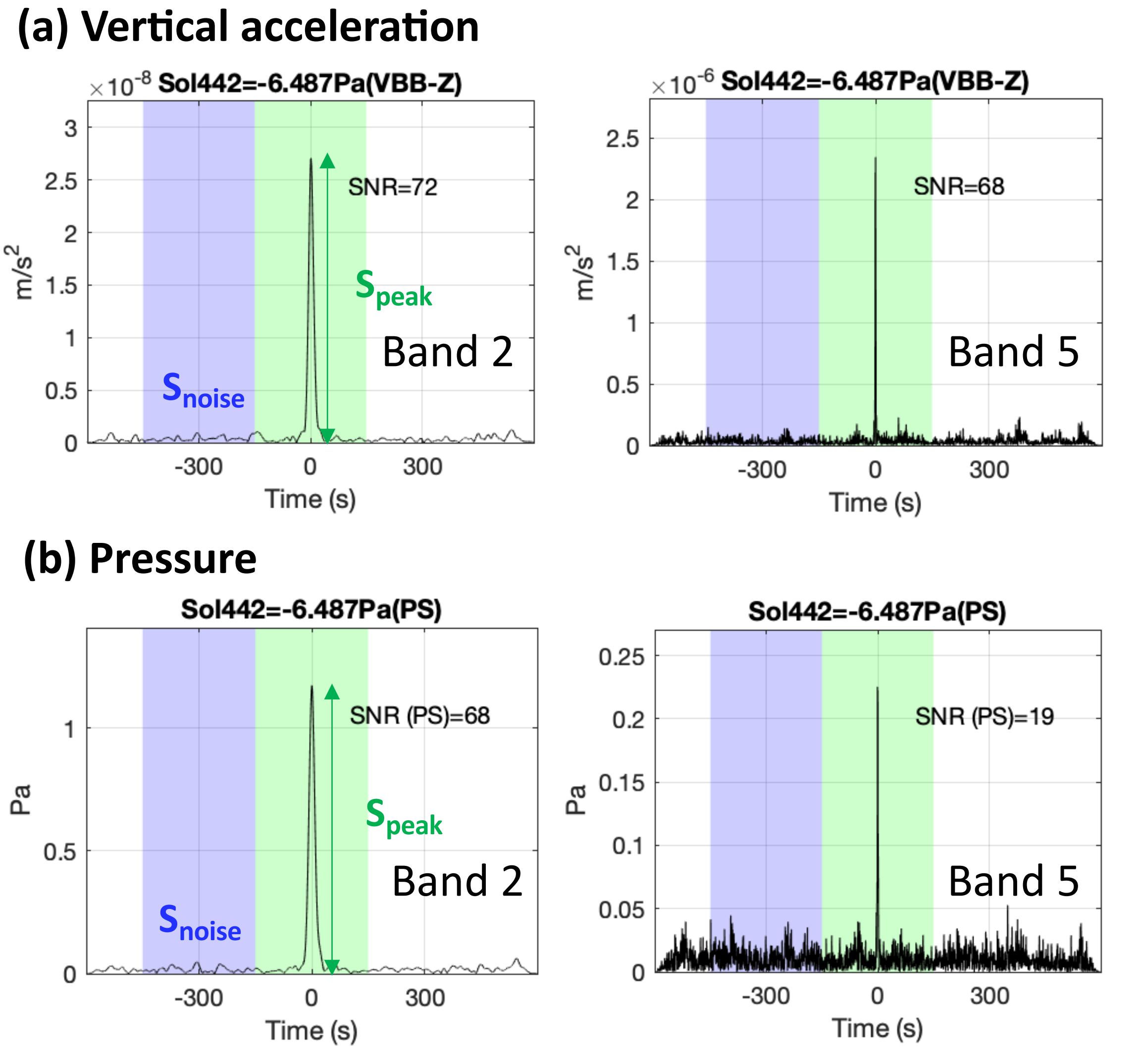

(a) Vertical acceleration
×10^-8 Sol442=-6.487Pa(VBB-Z)
m/s^2
SNR=72
S peak
S noise
Band 2
Time (s)
×10^-6 Sol442=-6.487Pa(VBB-Z)
SNR=68
Band 5
(b) Pressure
Sol442=-6.487Pa(PS)
Pa
SNR (PS)=68
S peak
S noise
Band 2
Time (s)
Sol442=-6.487Pa(PS)
SNR (PS)=19
Band 5

Figure5.

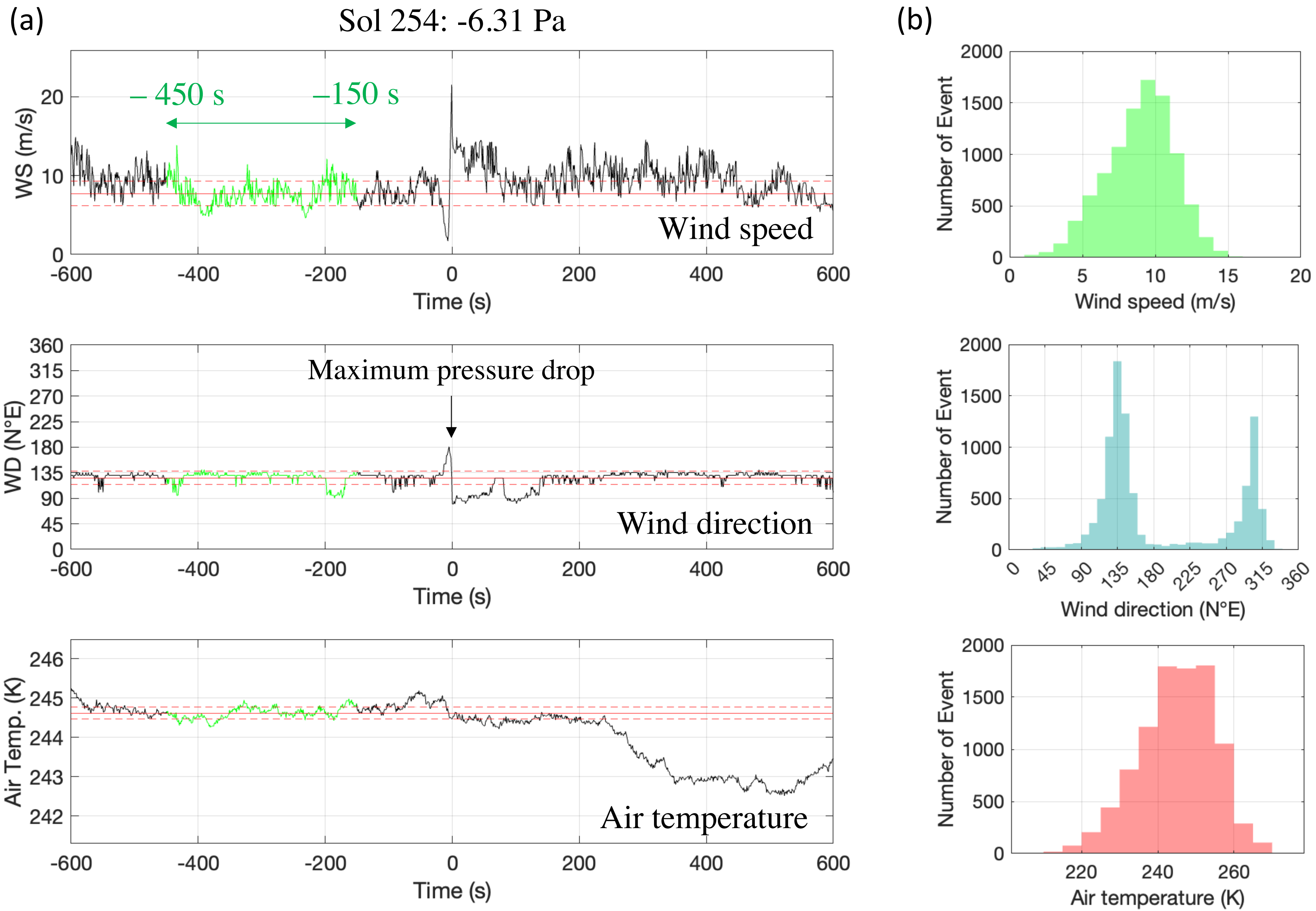

(a)
Sol 254: -6.31 Pa
– 450 s
–150 s
WS (m/s)
Wind speed
Time (s)
Maximum pressure drop
WD (N°E)
Wind direction
Time (s)
Air Temp. (K)
Air temperature
Time (s)
(b)
Number of Event
Wind speed (m/s)
Number of Event
Wind direction (N°E)
Number of Event
Air temperature (K)

Figure6.

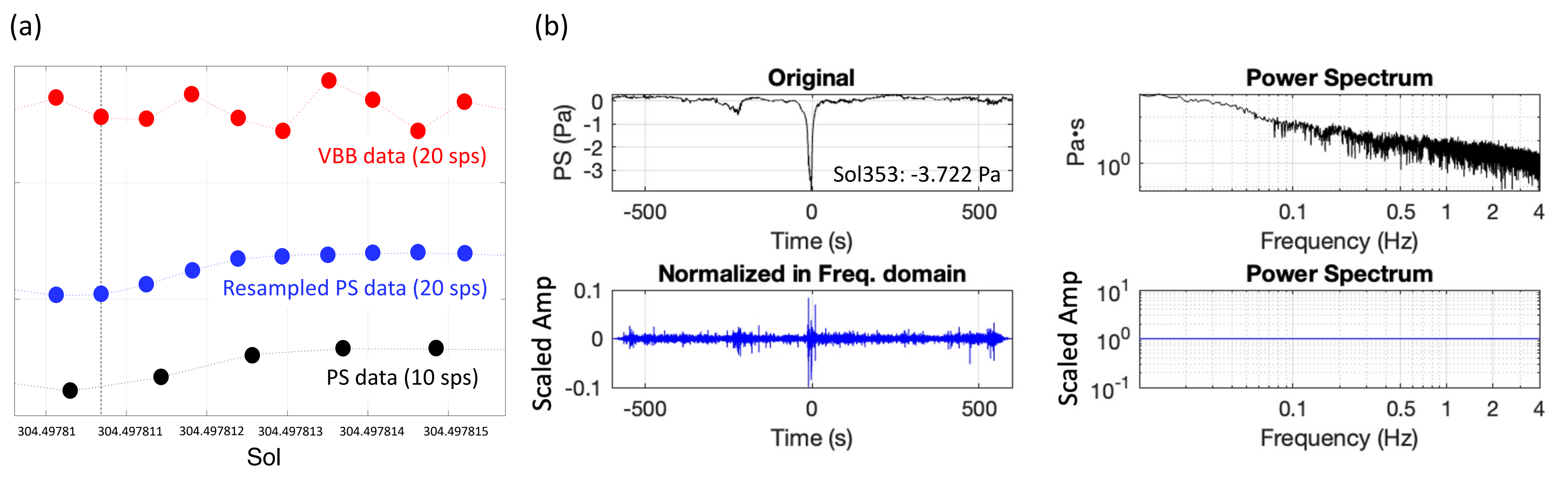
(a)
VBB data (20 sps)
Resampled PS data (20 sps)
PS data (10 sps)
304.49781
304.497811
304.497812
304.497813
304.497814
304.497815
Sol
(b)
Original
PS (Pa)
Sol353: -3.722 Pa
Time (s)
Power Spectrum
Pa•s
Frequency (Hz)
Normalized in Freq. domain
Scaled Amp
Time (s)
Power Spectrum
Scaled Amp
Frequency (Hz)

Figure7.

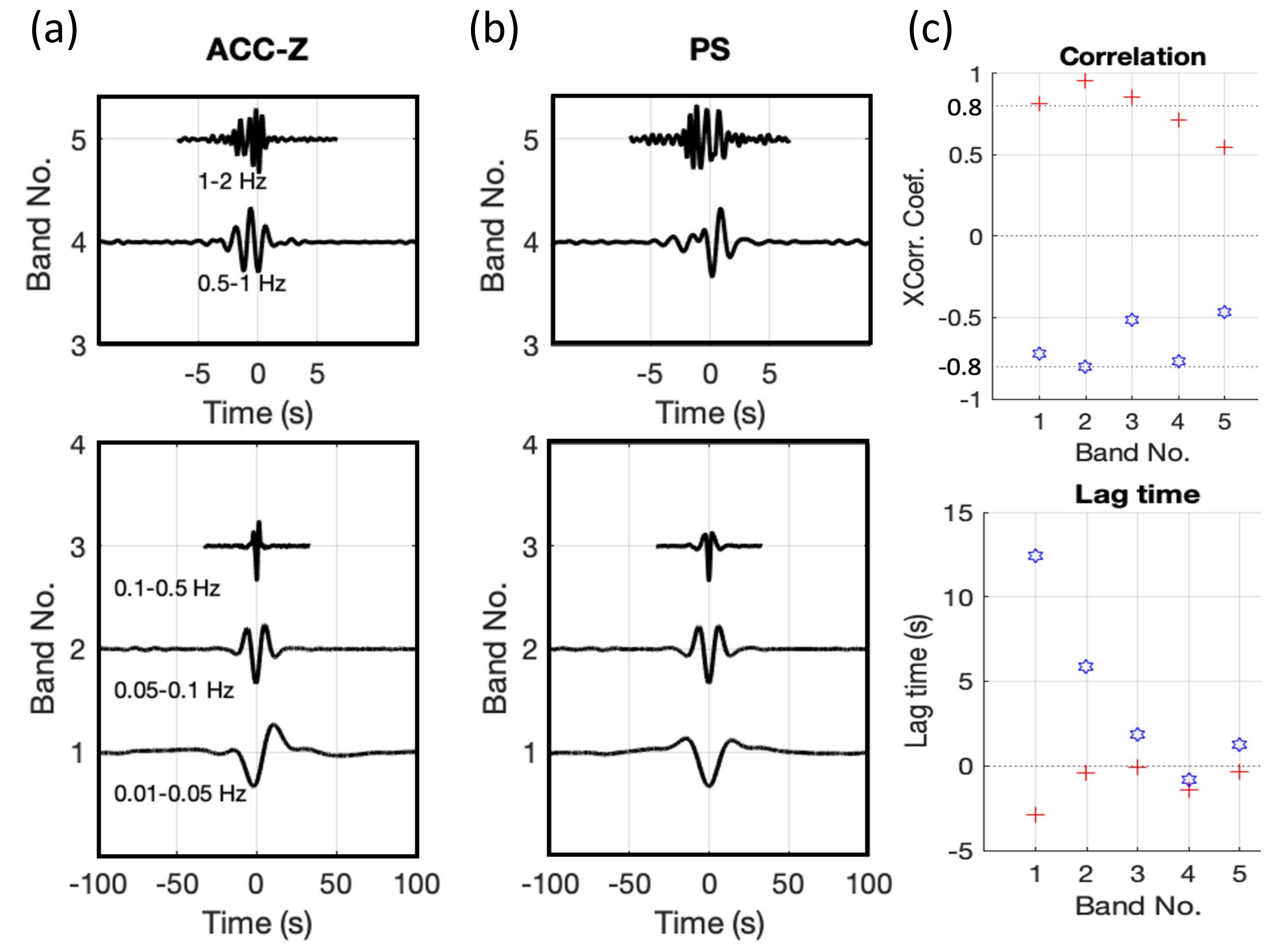

(a)
ACC-Z
Band No.
Time (s)
1-2 Hz
0.5-1 Hz
0.1-0.5 Hz
0.05-0.1 Hz
0.01-0.05 Hz
(b)
PS
Band No.
Time (s)
(c)
Correlation
XCorr. Coef.
Band No.
Lag time
Lag time (s)
Band No.

Figure8.

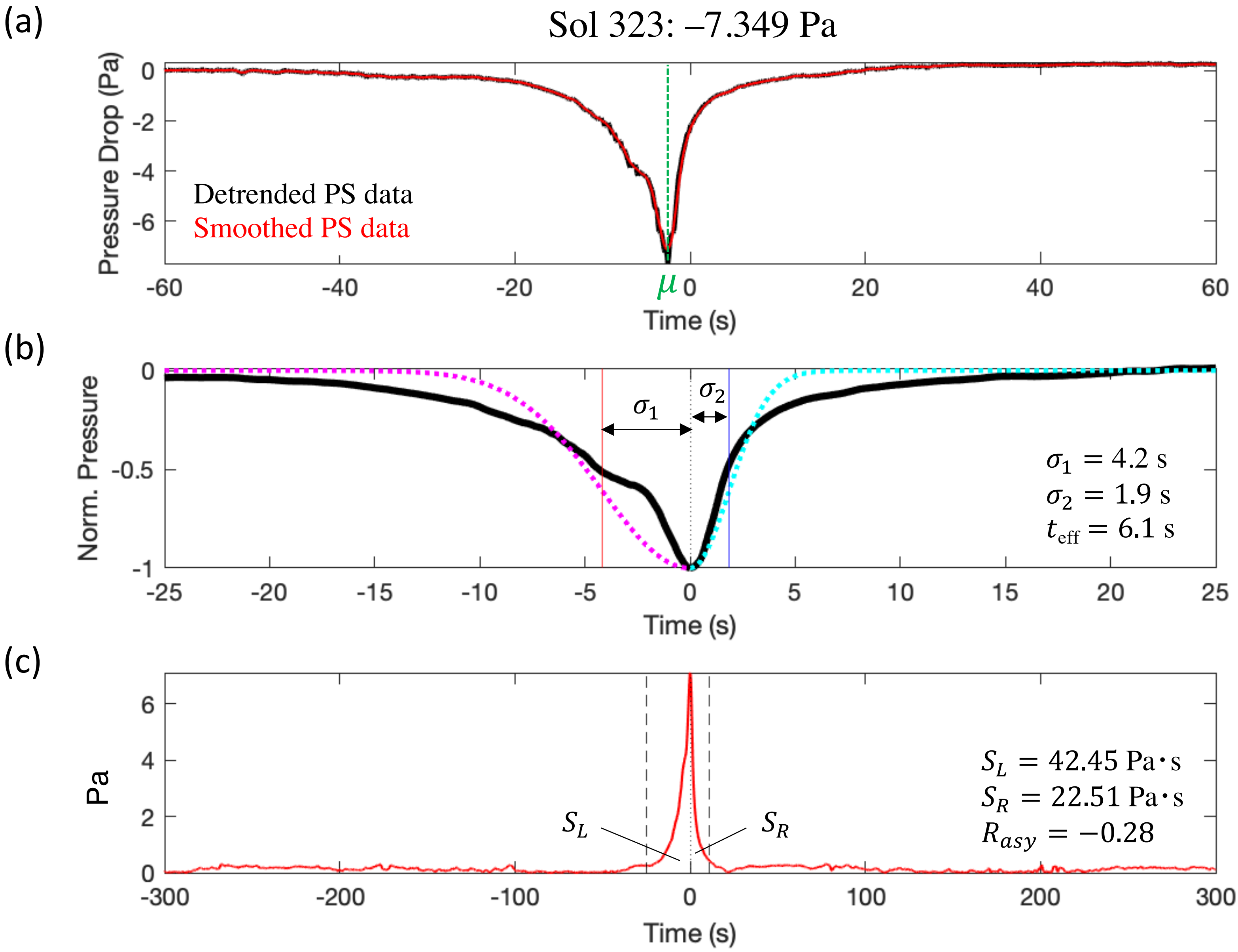

(a)
Sol 323: –7.349 Pa
Pressure Drop (Pa)
Detrended PS data
Smoothed PS data
μ
Time (s)
(b)
Norm. Pressure
σ1
σ2
σ1 = 4.2 s
σ2 = 1.9 s
t_eff = 6.1 s
Time (s)
(c)
Pa
S_L
S_R
S_L = 42.45 Pa·s
S_R = 22.51 Pa·s
R_asy = −0.28
Time (s)

Figure9.

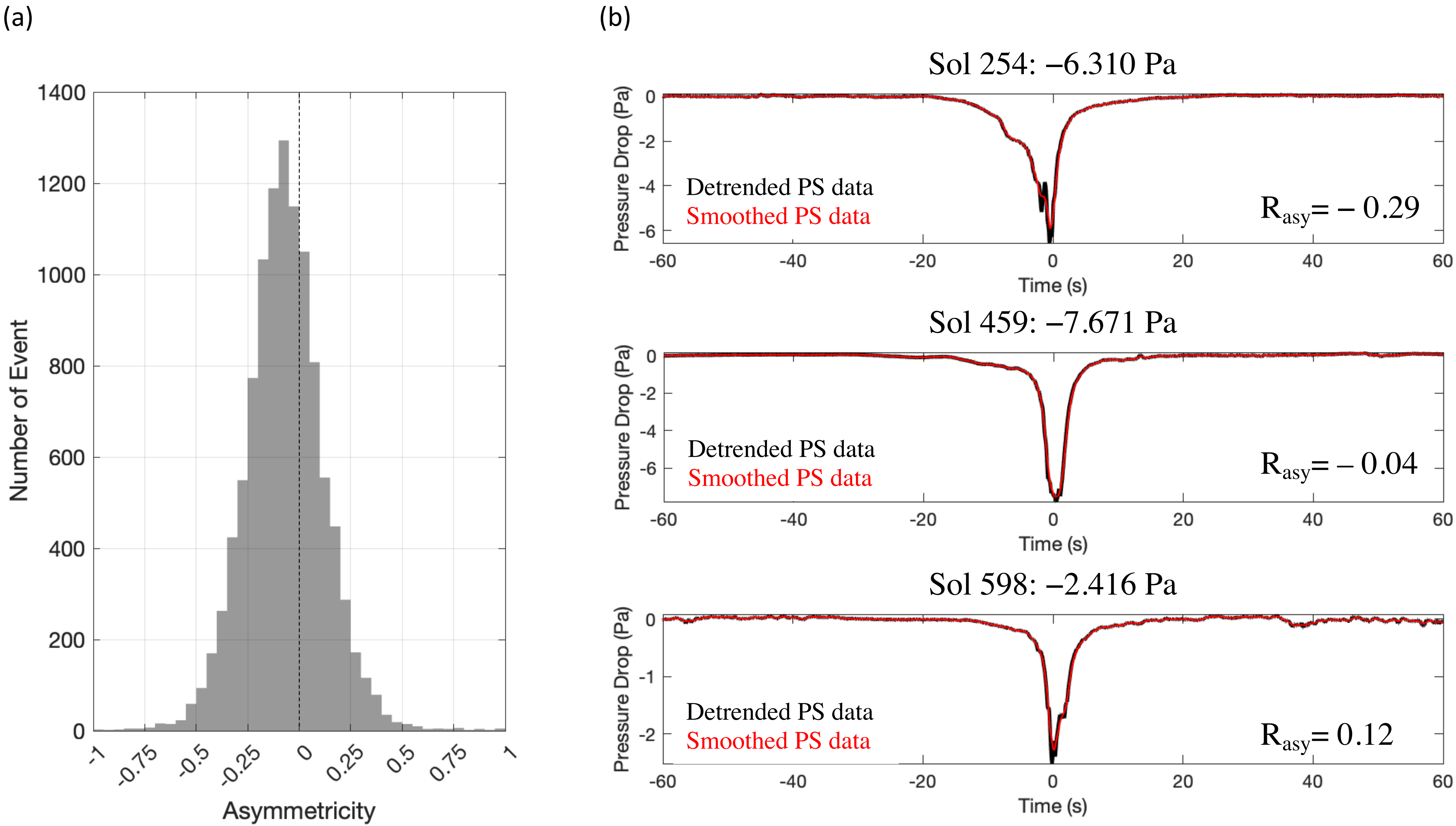
(a)
Number of Event
Asymmetricity
(b)
Sol 254: −6.310 Pa
Pressure Drop (Pa)
Time (s)
Detrended PS data
Smoothed PS data
R_{asy}= − 0.29
Sol 459: −7.671 Pa
Pressure Drop (Pa)
Time (s)
Detrended PS data
Smoothed PS data
R_{asy}= − 0.04
Sol 598: −2.416 Pa
Pressure Drop (Pa)
Time (s)
Detrended PS data
Smoothed PS data
R_{asy}= 0.12

Figure10.

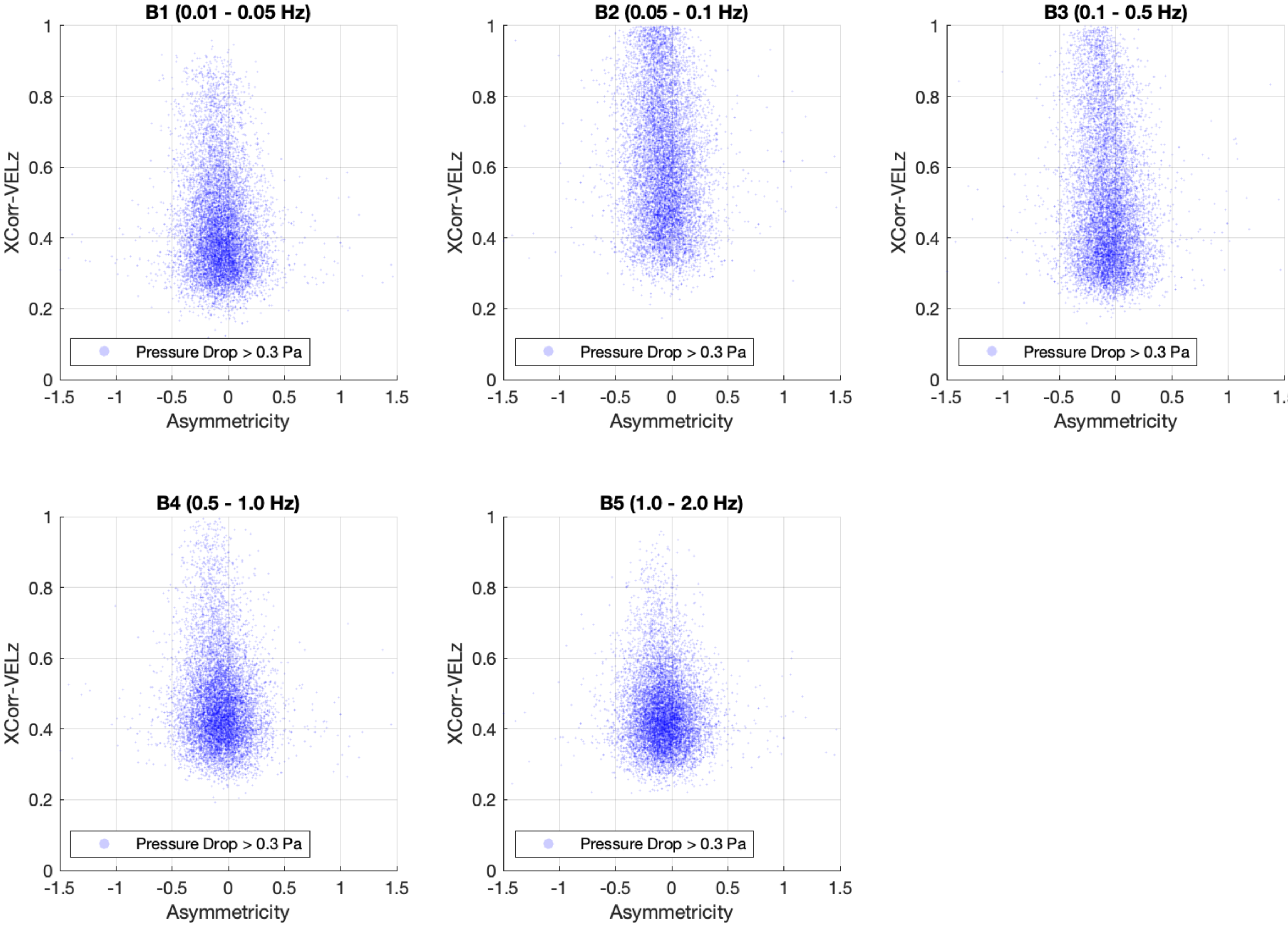

B1 (0.01 - 0.05 Hz)
B2 (0.05 - 0.1 Hz)
B3 (0.1 - 0.5 Hz)
B4 (0.5 - 1.0 Hz)
B5 (1.0 - 2.0 Hz)
XCorr-VELz
Asymmetricity
Pressure Drop > 0.3 Pa
1
0.8
0.6
0.4
0.2
0
-1.5
-1
-0.5
0
0.5
1
1.5

Figure11.

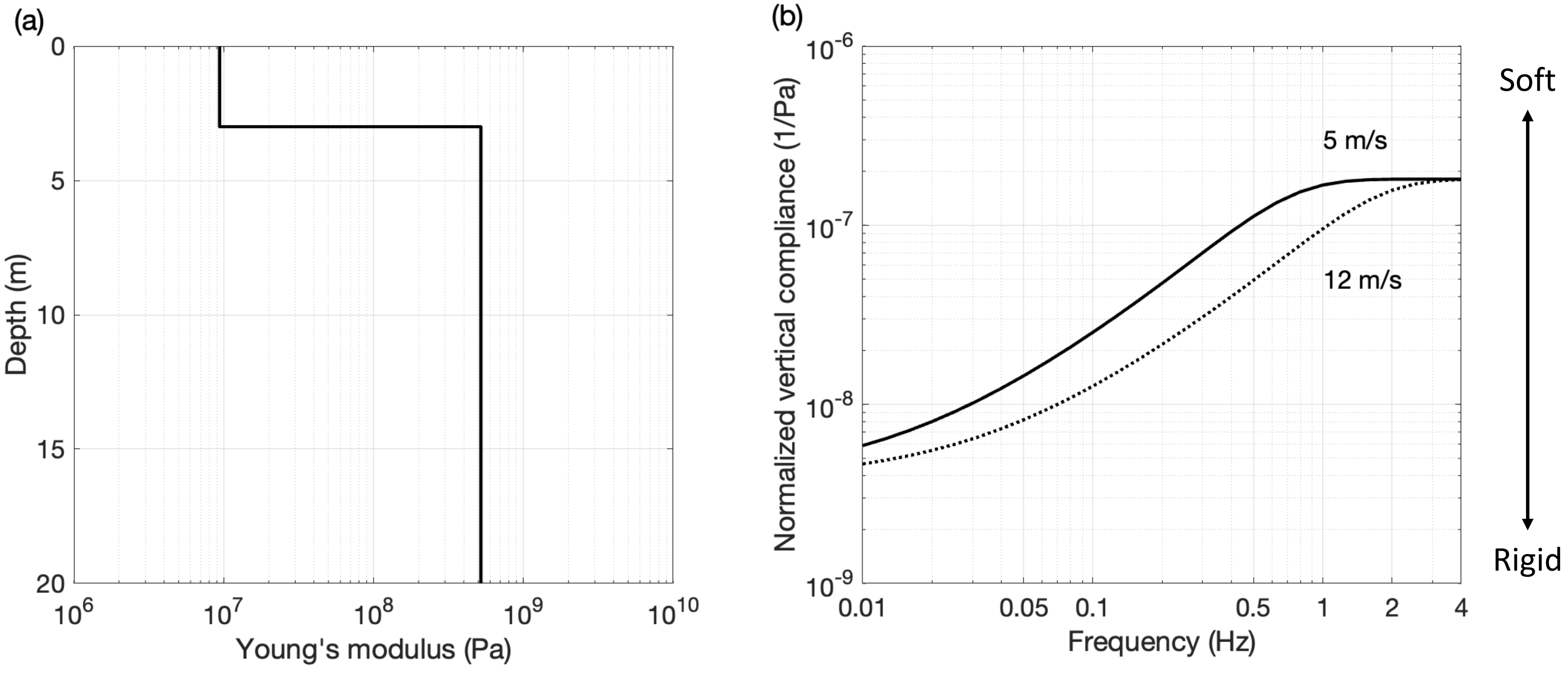
(a)
Depth (m)
0
5
10
15
20
10^6
10^7
10^8
10^9
10^{10}
Young's modulus (Pa)
(b)
Normalized vertical compliance (1/Pa)
10^{-6}
10^{-7}
10^{-8}
10^{-9}
0.01
0.05
0.1
0.5
1
2
4
Frequency (Hz)
5 m/s
12 m/s
Soft
Rigid

Figure12.

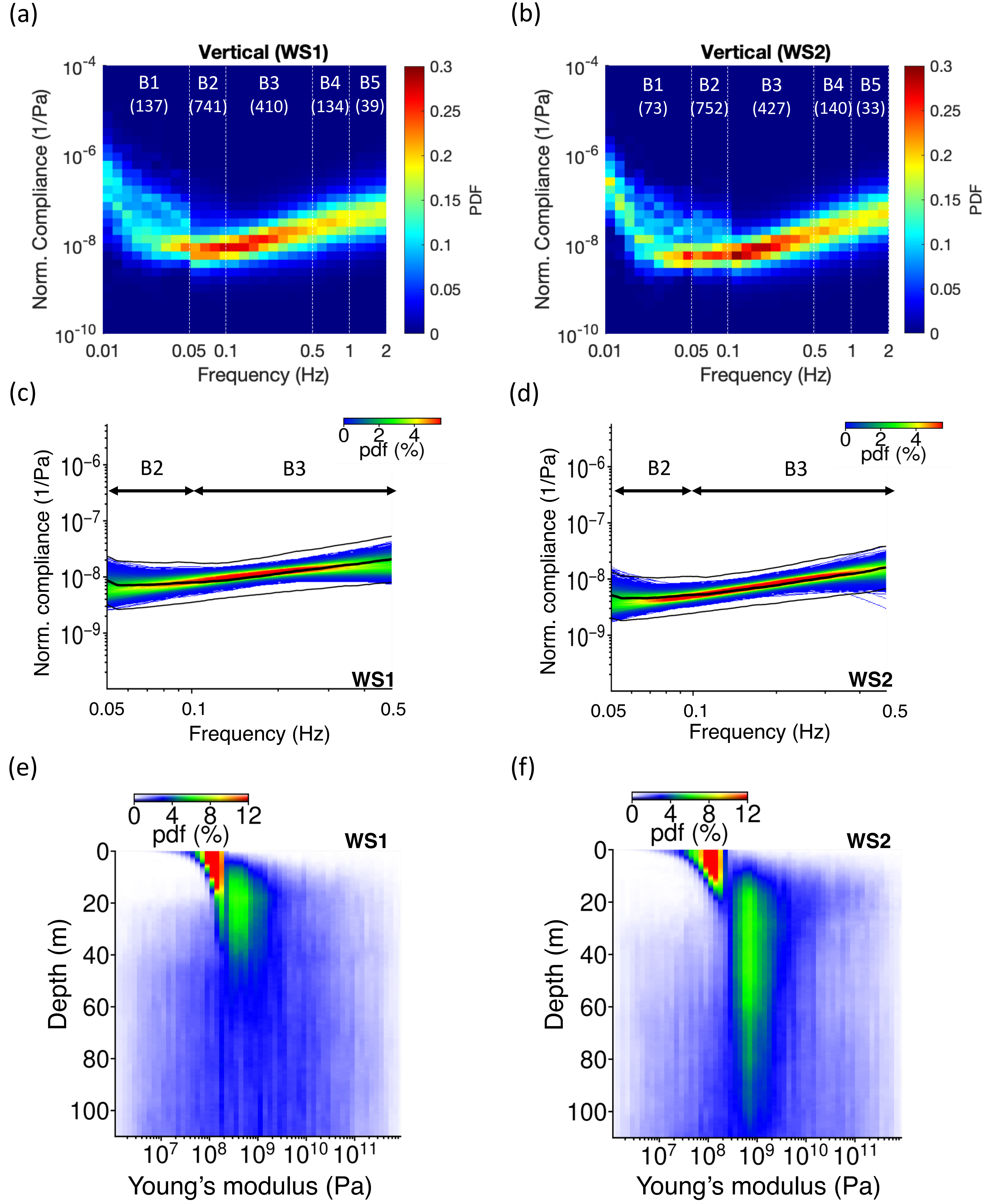

(a)
Vertical (WS1)
B1 (137)
B2 (741)
B3 (410)
B4 (134)
B5 (39)
Norm. Compliance (1/Pa)
10^{-4}
10^{-6}
10^{-8}
10^{-10}
0.01
0.05
0.1
0.5
1
2
Frequency (Hz)
PDF
0
0.05
0.1
0.15
0.2
0.25
0.3
(b)
Vertical (WS2)
B1 (73)
B2 (752)
B3 (427)
B4 (140)
B5 (33)
(c)
B2
B3
pdf (%)
Norm. compliance (1/Pa)
10^{-6}
10^{-7}
10^{-8}
10^{-9}
WS1
0.05
0.1
0.5
Frequency (Hz)
(d)
WS2
(e)
0
4
8
12
pdf (%)
Depth (m)
20
40
60
80
100
10^{7}
10^{8}
10^{9}
10^{10}
10^{11}
Young's modulus (Pa)
(f)

FigureB1.

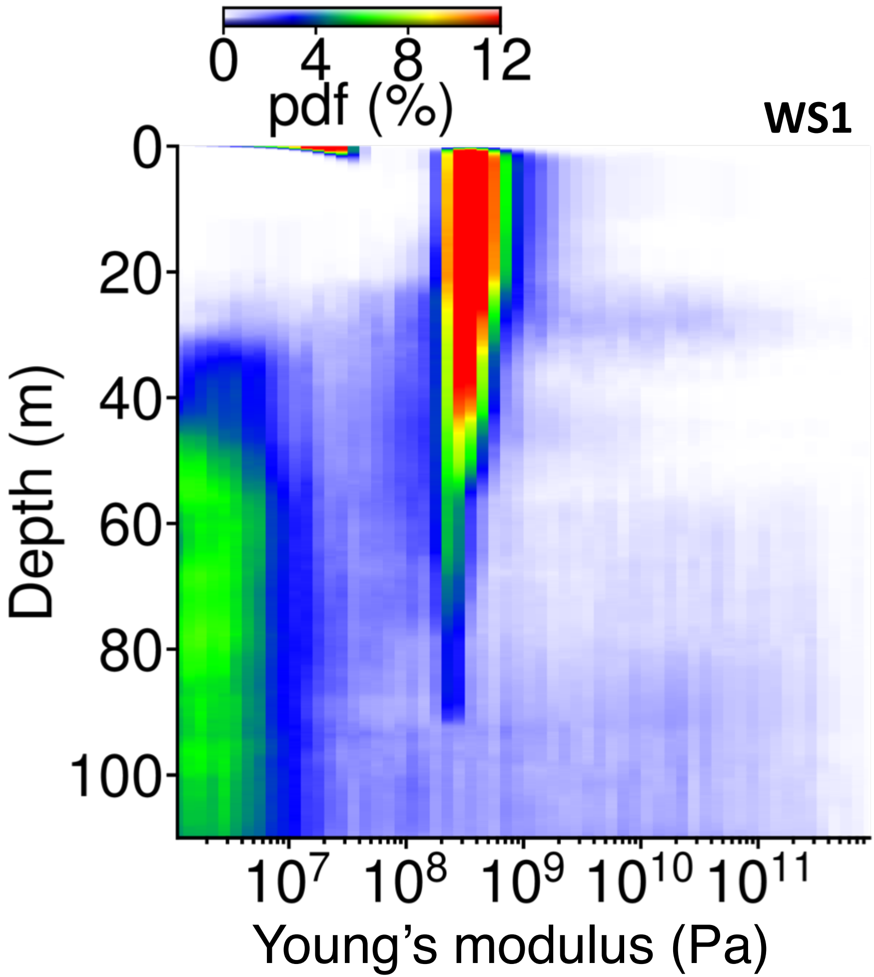

0
4
8
12
pdf (%)
WS1
Depth (m)
0
20
40
60
80
100
10^7
10^8
10^9
10^{10}
10^{11}
Young's modulus (Pa)

FigureC1.

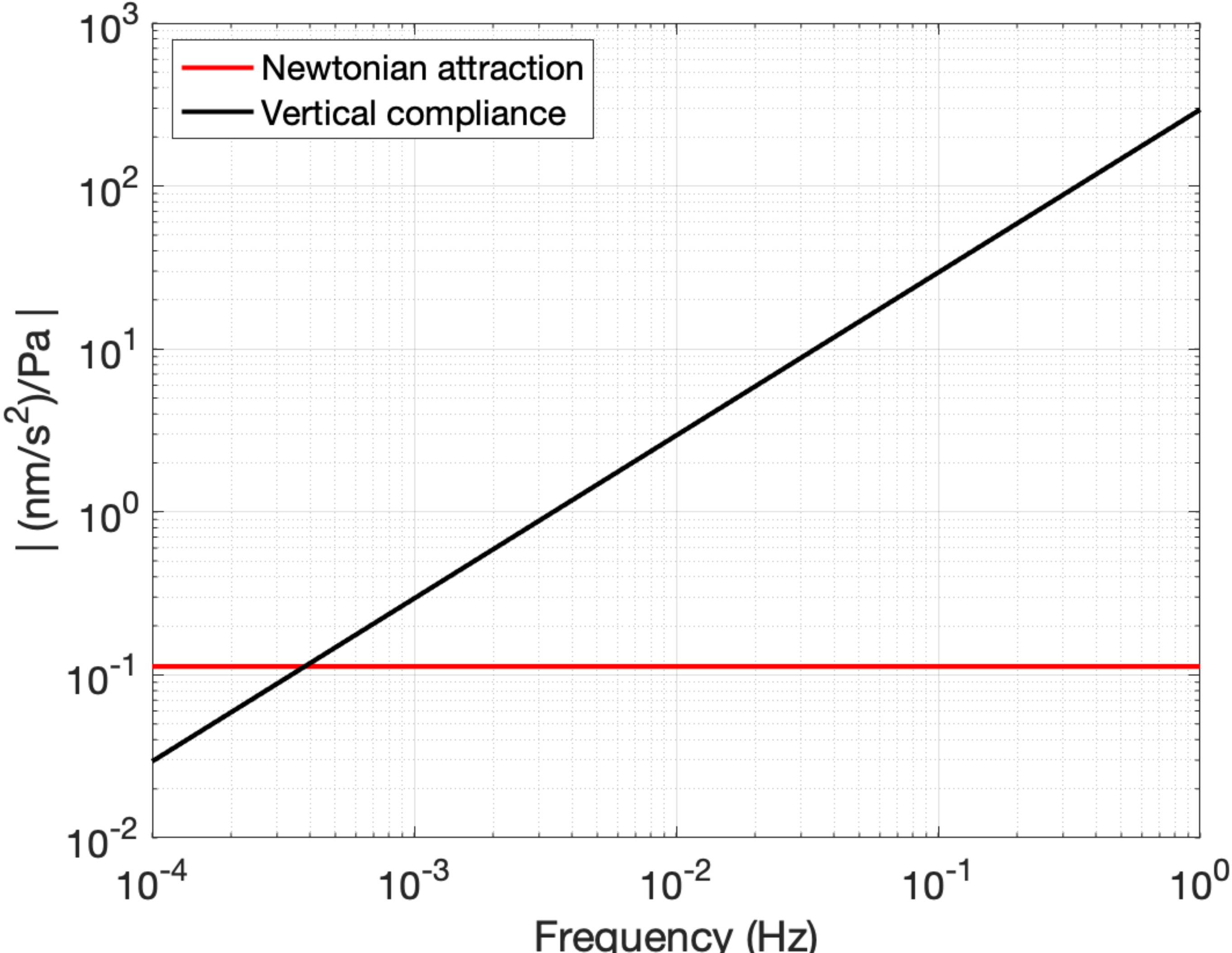

Newtonian attraction
Vertical compliance
| (nm/s^2)/Pa |
Frequency (Hz)
10^3
10^2
10^1
10^0
10^{-1}
10^{-2}
10^{-4}
10^{-3}
10^{-2}
10^{-1}
10^0